LIBRARY
MS #185

OAK RIDGE NATIONAL LABORATORY
operated by
UNION CARBIDE CORPORATION
NUCLEAR DIVISION
for the
U.S. ATOMIC ENERGY COMMISSION

169
1-8-75

ORNL-TM-3438

COPY NO. -

DATE - August 18, 1971

N75-70756
Unclas
00/98 07642
(NASA-CR-142002) LOW-ENERGY ELECTRON TRANSPORT BY THE METHOD OF DISCRETE ORDINATES Ph.D. Thesis - Missouri Univ. (Oak Ridge National Lab.) 104 p

Neutron Physics Division

LOW-ENERGY ELECTRON TRANSPORT BY THE METHOD OF DISCRETE ORDINATES*

D. E. Bartine,† R. G. Alsmiller, Jr., F. R. Mynatt,
W. W. Engle, Jr., and J. Barish†

(DISSERTATION)

Abstract

The one-dimensional discrete ordinates code ANISN has been adapted to simulate the transport of low-energy (on the order of a few MeV) electrons. Two different calculational techniques have been utilized for the treatment of electron-electron collisions that result in a small energy transfer. One method treats such collisions by a continuous slowing-down approximation, while the other method treats these collisions by the use of a very approximate cross section. Calculated results obtained with ANISN are compared with experimental data for the transmitted energy and angular distributions for 1-, 2.5-, 4-, and 8-MeV electrons normally incident on aluminum slabs of various thicknesses and for 1-MeV electrons normally incident on a gold slab. The calculated and experimental results are in reasonably good agreement for the aluminum slabs but are in poor agreement for the gold slab. Calculated results obtained with ANISN are also compared with calculated results obtained with Monte Carlo methods.

NOTE:
Research funded by
NATIONAL AERONAUTICS AND SPACE ADMINISTRATION
under Order H-38280A

*This paper has been submitted by D. E. Bartine to the University of Missouri-Rolla in partial fulfillment of the requirements for the degree of Doctor of Philosophy.

†Mathematics Division.

NOTICE This document contains information of a preliminary nature and was prepared primarily for internal use at the Oak Ridge National Laboratory. It is subject to revision or correction and therefore does not represent a final report.

07642

This report was prepared as an account of work sponsored by the United States Government. Neither the United States nor the United States Atomic Energy Commission, nor any of their employees, nor any of their contractors, subcontractors, or their employees, makes any warranty, express or implied, or assumes any legal liability or responsibility for the accuracy, completeness or usefulness of any information, apparatus, product or process disclosed, or represents that its use would not infringe privately owned rights.

TABLE OF CONTENTS

		Page
LIST OF ILLUSTRATIONS		v
I.	INTRODUCTION	1
II.	LITERATURE SURVEY	3
III.	DISCRETE ORDINATES TRANSPORT EQUATIONS	9
IV.	TRANSPORT CROSS-SECTION DATA	30
	A. Inelastic Electronic Scattering from Atomic Electrons	30
	B. Elastic Coulomb Scattering from Atomic Nuclei	37
	C. Bremsstrahlung (Radiative) Interactions with Nuclei and Atomic Electrons	38
	D. Photon Interactions	40
V.	COMPARISON WITH THEORETICAL MODELS	41
	A. Elastic Multiple-Scattering Angular Distribution	41
	B. Inelastic-Scattering Energy Distribution	41
VI.	COMPARISON WITH EXPERIMENTAL RESULTS	51
	A. Experiments of Rester	51
	1. 1-MeV Electrons Incident on Aluminum	51
	2. 1-MeV Electrons Incident on Gold	61
	3. 2.5-MeV Electrons Incident on Aluminum	64
	B. Experiments of Lonergan *et al.*	69
	1. 4-MeV Electrons Incident on Aluminum	69
	2. 8-MeV Electrons Incident on Aluminum	72
VII.	COMPARISON WITH A THEORETICAL CALCULATION FOR AN INCIDENT ELECTRON SPECTRUM	75
	A. Transmitted Electron Spectra	75
	B. Transmitted Photon Spectra	78
VIII.	CONCLUSIONS AND RECOMMENDATIONS	80

(continued)

TABLE OF CONTENTS (cont'd)

Page

IX. APPENDICES 82

A. Derivation of the Continuous Slowing-Down Transport Equation 83

B. High-Frequency End-Point Correction for the Differential Bremsstrahlung Cross Section 89

ACKNOWLEDGMENTS 92

REFERENCES 93

LIST OF ILLUSTRATIONS

Figures Page

1. Angular distribution of transmitted electron current for 1-MeV electrons normally incident on a 0.0287-g/cm^2-thick aluminum slab 42

2. Comparison of the differential Møller cross section for inelastic electron-electron collisions with two differential analytic cross sections below 1 MeV 46

3. Transmitted electron current per unit energy per incident electron for 1-MeV electrons normally incident on 0.11-g/cm^2-thick and 0.33-g/cm^2-thick aluminum slabs 48

4. Transmitted electron current per unit energy per incident electron for 1-MeV electrons normally incident on 0.11-g/cm^2-, 0.33-g/cm^2-, and 0.66-g/cm^2-thick aluminum slabs 50

5. Transmitted electron current per unit energy per incident electron for 1-MeV electrons normally incident on 0.10-g/cm^2-, 0.22-g/cm^2-, and 0.32-g/cm^2-thick aluminum slabs 52

6. Transmitted electron current per unit energy per incident electron for 1-MeV electrons normally incident on 0.22-g/cm^2-thick aluminum slabs 55

Figures Page

7. Energy distributions of the transmitted electron current at 7.5°, 47.5°, and 77.5° for 1-MeV electrons normally incident on a 0.10-g/cm^2-thick aluminum slab 59

8. Energy distributions of the transmitted electron current at 7.5°, 47.5°, and 77.5° for 1-MeV electrons normally incident on a 0.22-g/cm^2-thick aluminum slab 60

9. Angular distributions of the transmitted electron current for 1-MeV electrons normally incident on 0.10-g/cm^2-, 0.22-g/cm^2-, and 0.32-g/cm^2-thick aluminum slabs 62

10. (a) Transmitted electron current per unit energy per incident electron for 1-MeV electrons normally incident on a 0.15-g/cm^2-thick gold slab.

(b) Angular distribution of the transmitted electron current for 1-MeV electrons normally incident on a 0.15-g/cm^2-thick gold slab. 63

11. Transmitted electron current per unit energy per incident electron for 2.5-MeV electrons normally incident on 0.31-g/cm^2-thick and 0.62-g/cm^2-thick aluminum slabs 65

Figures . Page

12. Energy distributions of the transmitted electron current at 20°, 45°, and 60° for 2.5-MeV electrons normally incident on a 0.31-g/cm^2-thick aluminum slab. 67

13. Energy distributions of the transmitted electron current at 10° and 20° for 2.5 MeV electrons normally incident on a 0.62-g/cm^2-thick aluminum slab. 68

14. Angular distributions of the transmitted electron current for 2.5-MeV electrons normally incident on 0.31-g/cm^2-thick and 0.62-g/cm^2-thick aluminum slabs. 70

15. (a) Energy distribution of the transmitted electron current at 30° for 4-MeV electrons normally incident on a 1.275-g/cm^2-thick aluminum slab.

(b) Angular distributions of the transmitted electron current for 4-MeV electrons normally incident on a 1.275-g/cm^2-thick aluminum slab 71

16. (a) Energy distribution of the transmitted electron current at 20° for 8-MeV electrons normally incident on a 0.953-g/cm^2-thick aluminum slab.

(b) Angular distribution of the transmitted electron current for 8-MeV electrons normally incident on a 0.953-g/cm^2-thick aluminum slab 73

Figures Page

17. Energy distribution of the incident electron current per unit energy per incident electron used by Scott[48] as a source. 76

18. Transmitted electron current per unit energy per incident electron for a specific energy spectrum (Fig. 17) normally incident on 0.50-g/cm^2-thick and 1.0-g/cm^2-thick aluminum slabs. 77

19. Transmitted photon current per unit energy per incident electron for a specific energy spectrum of electrons (Fig. 17) normally incident on aluminum slabs of the thicknesses indicated. 79

I. INTRODUCTION

The men and instruments aboard space vehicles must be protected from the radiation encountered in extra-terrestrial flight. A significant research effort has been under way for some time to discover the identity, energy, and abundance of the particles involved, and to determine their ability to penetrate shielding materials.[1,2] A manned space laboratory orbiting through the Van Allen electron belts would be exposed to a large number of low-energy electrons. A code is available that treats low-energy electron transport by Monte Carlo methods.[3] However, because of difficulties with the statistical accuracy obtained in some cases, a nonstatistical calculational method is needed. The purpose of this investigation is to study the adaptability of the method of discrete ordinates, which was developed for neutron transport, to the transport of low-energy electrons and the photons which they produce.

Consideration here is limited to the energy range below 10 MeV, since this is the area of primary concern for the shielding of space vehicles. However, this energy range is broad enough to be of general interest. Other problems to which the calculational method developed here might be applied include the effect of multiple scattering on the response of beta detectors and the effect of the energy fluctuations resulting when a monoenergetic beam of electrons is incident on a thin target (for example, in a device such as the electron microscope).

In Section II a basic discussion of electron penetration is presented, and previous efforts made toward the solution of this problem are reviewed. The equations involved in the methods of solution used in this investigation are given in Section III. The specific forms of the cross sections and other parameters utilized in the equations are discussed in Section IV. Comparisons between the results obtained from this investigation and results from other sources, both calculational and experimental, are presented in Sections V, VI, and VII. A pure angular spectrum from multiple elastic scattering and a pure energy spectrum due to electron straggling are considered in Section V, and comparisons with experimental results are given in Section VI. Experimental data are limited, and none were available to describe the penetration of an incident energy spectrum such as that incident on spacecraft in the Van Allen belts. A comparison with another calculational method for the electron energy distribution resulting from a fission spectrum source of electrons is presented in Section VII. Energy spectra for the photons produced by these electrons and transported through large slab thicknesses are also included here. Conclusions and recommendations for further investigation are discussed in Section VIII. The detailed derivation of the transport equation with a term corresponding to the continuous slowing-down approximation is given in Appendix A, and the derivation of the high-frequency end-point correction applied to the bremsstrahlung cross section is shown in Appendix B.

II. LITERATURE SURVEY

When electrons with energies of a few MeV penetrate matter, they undergo a large number of collisions within a very short pathlength. Since there are many possible energy and angular changes for each collision, this results in a distribution of electrons in terms of both energy and direction of travel. The most significant interactions for the prediction of the resulting distribution by transport calculations are elastic nuclear (Coulomb) scattering, inelastic scattering from atomic electrons, and radiative (bremsstrahlung) interactions with both nuclei and atomic electrons. Birkhoff[4] described electronic interactions and summarized the progress made on numerical models representing various aspects of electron transport. More recently, Zerby and Keller[5] presented a comprehensive state-of-the-art review of theoretical and experimental investigations in the area of electron transport.

Coulomb interactions are very frequent, resulting in an angular distribution heavily peaked in the forward direction. Since the mass of the electron is minute compared to that of the nucleus, the energy loss suffered by the electron is insignificant, and these collisions may be considered elastic. Various methods have been developed for calculating multiple — (Coulomb) scattering distributions. Molière[6,7] formulated a numerical function in terms of a reduced scattering angle to describe the result of small angular deflections. Goudsmit and Saunderson[5,8] derived a Legendre series that can be evaluated for a specific single-scattering cross section to give the distribution resulting from angular deflections of any magnitude.

Electronic collisions with atomic electrons resulting in a small energy transfer and a correlated small angular deflection are also quite numerous. The atomic electron involved is either elevated to an excited state or ionized if the energy transfer is sufficiently great. Collisions involving a large energy transfer and angular deflection do occur, but their frequency decreases as a function of increasing energy loss. The secondary or knock-on electron produced in such a collision becomes part of the transmitted spectrum. High energy-loss reactions are therefore particularly important for an accurate determination of the electron flux resulting at thicknesses approaching the range of the incident beam. Inelastic scattering from atomic electrons is the primary mode of energy loss for electrons in the few MeV range. Williams[9,10] and Landau[11] derived a universal curve to describe the characteristic distribution of energies resulting when a monoenergetic electron beam passes through a thin foil; i.e., one in which the average energy loss is small compared to the initial energy of the electron. Angular effects were not considered. The curve is basically a Gaussian distribution centered near the most probable energy loss with a long tail at lower energies. Collisions involving a small energy transfer are responsible for the Gaussian distribution, while larger energy transfers cause the tail. Blunck and Leisegang[12,13] give a correction for the Landau theory to account for the effect of more tightly bound atomic electrons, especially the K-shell electrons for high-Z atoms. Vavilov[14,15] modified the Landau distribution to make it more indicative of the incident-particle velocity.

Bremsstrahlung reactions also result in energy degradation, although they are not of prime interest in the range considered here. Bremsstrahlung becomes much more significant as the electron energy and the atomic number of the target increase. However, bremsstrahlung reactions are crucial in the determination of radiation effects at target depths beyond the range of the incident electrons. Koch and Motz[16] present a detailed review of the bremsstrahlung interaction.

Various attempts have been made to solve the complete electron-transport problem by applying numerical techniques that combine the results of several existing theories. In contrast to any of the theories previously mentioned, such calculations distinguish between electron pathlength and sample thickness.

The moments method is a semianalytical numerical solution to the transport equation in which the energy, angular, and spatial dependence of the flux are described by a series of polynomial expansions. Spencer and Fano[12] adapted the moments method to the electron transport problem. Electron-electron collisions involving small energy transfers were treated according to a continuous slowing-down model which assumes that the form of the cross sections for these collisions is unimportant as long as the correct stopping power (energy loss per unit path length) is obtained. Specifically, the relativistic Møller[17] cross section for electronic collisions with free electrons at rest is assumed to be valid down to a very small fractional energy loss which is defined so as to give the correct total stopping power. Spencer and Fano's method assumes an infinite, homogeneous medium and

includes the production of secondary or knock-on electrons. Photon production via bremsstrahlung reactions is accounted for, but there is no provision for subsequent transport of the photons.

Theoretically, Monte Carlo calculations can follow each individual electron through every collision as the electrons are slowed down and scattered through the target foil. In practice, this is not feasible due to the staggering number of collisions involved. A single electron with an initial energy of a few MeV will undergo in the neighborhood of 10^5 collisions in the process of downscattering to the 0.1 MeV range. Individual electronic collisions are therefore not treated in the Monte Carlo calculations. Instead, theories describing various segments of the transport problem are used to group together large numbers of collisions. The computation proceeds by considering successive spatial intervals, with the resulting distributions determined by a conventional random sampling based on the suitable multiple-scattering theories.[18] Berger and Seltzer[3] have written a Monte Carlo code ETRAN, in which the angular deflections can be computed by the method of Goudsmit and Saunderson, Molière, or Fermi's Gaussian distribution. The spectrum resulting from energy loss is determined by the modified Landau energy-straggling distribution or from a continuous slowing-down model. Collisions involving large energy transfers can be considered separately from the continuous slowing-down model, and secondary electrons and photons are produced and transported through the target sample.[18] In general, calculations based on

ETRAN have shown good agreement with experimental results.[5] Nevertheless, the Monte Carlo method is restricted by the statistical variations inherent in random sampling.

The method of discrete ordinates offers a viable alternative to Monte Carlo methods in that it can follow each electron on a collision-by-collision basis, it does not involve random sampling, and it requires only basic cross-section data. In the original discrete ordinates method for slab geometry as suggested by Wick,[19,20] the angular variable is divided into a discrete number of intervals. The transfer integral term in the Boltzmann transport equation is then approximated by a Gaussian quadrature formula, resulting in a set of coupled equations for the discrete-angle fluxes. The S_n method is a special case of the discrete ordinates method developed by Carlson.[21] Here, the directional flux is assumed to vary linearly between interpolation points in both the angular and spatial variables. Carlson later simplified and generalized the S_n method into the current discrete ordinates method.[22] The flux is now stated in terms of the average values at the midpoints of the spatial and angular intervals. The discrete ordinates method was developed for neutron transport and is now preferentially used for the solution of one- and two-dimensional neutron- and gamma-transport problems in the form of codes such as ANISN[23] and DOT.[24] This investigation is the first attempt to adapt discrete ordinates procedures for the transport of electrons through matter. In principle, ANISN may be used to transport electrons by the simple expedient of introducing into the code the differential cross sections for

electron-nucleus elastic collisions, electron-nucleus bremsstrahlung-producing collisions, and electron-electron collisions. In practice, however, these cross sections are quite different from those which occur in neutron transport, and the method has shown only partial success in transporting electrons. The discrete ordinates method allows the production of photons and secondary electrons, and their subsequent transport through the target. Individual electronic collisions are treated except in the continuous slowing-down version of electron transport by discrete ordinates where electron-electron collisions that result in a small energy transfer are handled by a continuous slowing-down term.

Experimentally obtained electron-transmission data provide a basis with which to test theoretical calculations. The energy spectra of electrons transmitted through slab targets have been measured as a function of angle. Rester and Rainwater[25] considered 1-MeV electrons normally incident on aluminum slabs. Rester and Dance[26] studied the spectra resulting from 1-MeV electrons on aluminum and gold targets. Lonergan, Jupiter, and Merkle[27] investigated the transmission of 4- and 8-MeV incident-electron beams through beryllium, aluminum, and gold targets.

III. DISCRETE ORDINATES TRANSPORT EQUATIONS

The equations used to transport electrons and photons through matter are developed in this section. The time-independent Boltzmann transport equation can be written for electrons in a uniform medium as

$$\vec{\Omega}\cdot\nabla\phi(\vec{R},E,\vec{\Omega}) = P(\vec{R},E,\vec{\Omega}) + n\int_E^{E_o} dE' \int d\Omega' \frac{d^2\sigma_{e\to e}}{dEd\Omega}(E',E,\vec{\Omega}'\cdot\vec{\Omega})\phi(\vec{R},E',\vec{\Omega}')$$

$$+ n\int_E^{E_o} dE' \int d\Omega' \frac{d^2\sigma_{\gamma\to e}}{dEd\Omega}(E',E,\vec{\Omega}'\cdot\vec{\Omega})\phi_\gamma(\vec{R},E',\vec{\Omega}') \qquad (1)$$

$$- n\,\sigma_e^T(E)\phi(\vec{R},E,\vec{\Omega}) ,$$

and for photons in a uniform medium as

$$\vec{\Omega}\cdot\nabla\phi_\gamma(\vec{R},E,\vec{\Omega}) = P_\gamma(\vec{R},E,\vec{\Omega}) - n\,\sigma_\gamma^T(E)\phi_\gamma(\vec{R},E,\vec{\Omega})$$

$$+ \int_E^{E_o} dE' \int d\Omega' \frac{d^2\sigma_{\gamma\to\gamma}}{dEd\Omega}(E',E,\vec{\Omega}'\cdot\vec{\Omega})\phi_\gamma(\vec{R},E',\vec{\Omega}') \qquad (2)$$

$$+ n\int_E^{E_o} dE' \int d\Omega' \frac{d^2\sigma_{\gamma\to\gamma}}{dEd\Omega}(E',E,\vec{\Omega}'\cdot\vec{\Omega})\phi(\vec{R},E',\vec{\Omega}') ,$$

$$\frac{d^2\sigma_{e\to e}(E',E,\vec{\Omega}'\cdot\Omega)}{dEd\Omega} = \sum_i \frac{d^2\sigma_i(E',E,\vec{\Omega}'\cdot\vec{\Omega})}{dEd\Omega}, \qquad i = e\ell,\ br,\ inel,$$

$$\sigma_i^T(E') = \int dE \int d\Omega \frac{d^2\sigma_i(E',E,\vec{\Omega}'\cdot\vec{\Omega})}{dEd\Omega},$$

$$\sigma_e^T(E') = \sum_i \sigma_i^T(E') \qquad i = e\ell,\ br,\ inel,$$

$$\frac{d^2\sigma_{\gamma\to\gamma}(E',E,\vec{\Omega}'\cdot\vec{\Omega})}{dEd\Omega} = \sum_i \frac{d^2\sigma_i(E',E,\vec{\Omega}'\cdot\vec{\Omega})}{dEd\Omega} \qquad i = co,\ pe,\ pp,$$

$$\sigma_\gamma^T(E') = \sum_i \sigma_i^T(E'), \qquad i = co,\ pe,\ pp,$$

where

$\vec{R}$ = a vector denoting the position of the particle;

$\vec{\Omega}$ = a unit vector in the direction of the momentum vector;

$d\Omega$ = an element of solid angle;

E' = the kinetic energy of the incident particle;

E = the kinetic energy of the emergent particle;

$\phi(\vec{R},E,\vec{\Omega})$ = the electron flux per unit energy;

$\phi_\gamma(\vec{R},E,\vec{\Omega})$ = the photon flux per unit energy;

E_o = the highest kinetic energy considered;

n = the atomic number density:

$P(\vec{R},E,\vec{\Omega})$ = the number of electrons per unit energy per steradian per unit volume per second input at R from an external source;

$P_\gamma(\vec{R},E,\vec{\Omega})$ = the number of photons per unit energy per steradian per unit volume per second input at R from an external source ($P_\gamma(\vec{R},E,\vec{\Omega}) = 0$ in the calculations undertaken here);

$\frac{d^2\sigma_i(E',E,\vec{\Omega}'\cdot\vec{\Omega})}{dEd\Omega}$ = the differential atomic cross section for a particle with kinetic energy E' going in direction $\vec{\Omega}'$ to undergo process i, after which the particle has a kinetic energy D and is traveling in direction $\vec{\Omega}$;

for electrons,

i = eℓ (elastic nuclear scattering, for which E' = E),

br (bremsstrahlung scattering from both nuclei and atomic electrons, thereby producing a photon),

inel (inelastic scattering from atomic electrons, thereby producing a secondary electron; the differential cross section here includes the production of both the primary and secondary electrons);*

---

*The inelastic scattering cross section used in this investigation is the atomic cross section, and is found by multiplying the differential cross section for an inelastic electron-electron collision by the number of electrons per atom, Z. An elastic electron-electron collision involving an incident electron with kinetic energy E' results in a primary electron with kinetic energy E and an energy loss of E'-E which is imparted to the struck electron. If E'-E is large enough, ionization occurs and a secondary electron is produced with kinetic energy E'-E, neglecting the energy required for the ionization process. If E'-E is too small for ionization, the struck electron is elevated to an excited state. However, because of a lack of cross-section information in the region where the energy imparted is on the order of the binding energy or less, it was necessary in this investigation to assume that a secondary electron is produced in each inelastic electron-electron collision,

so that the multiplicity for such collisions was 2. The differential cross section $\frac{d\sigma_{inel}}{dEd\Omega}(E',E,\vec{\Omega}'\cdot\vec{\Omega})$ in the equations in the text is always assumed to include both the primary and secondary electron; that is, integration of the differential inelastic cross section over energy and angle gives the total inelastic cross section times the multiplicity,

$$\nu_{inel}\ \sigma^{T}_{inel}\ (E') = \int_{o}^{E'} dE \int d\Omega\ \frac{d^2\sigma_{inel}\ (E',E,\vec{\Omega}'\cdot\vec{\Omega})}{dEd\Omega}\ .$$

Since the multiplicity is 2 by assumption,

$$\sigma^{T}_{inel}(E') = \frac{1}{2}\int_{o}^{E'} dE \int d\Omega\ \frac{d^2\sigma_{inel}\ (E',E,\vec{\Omega}'\cdot\vec{\Omega})}{dEd\Omega}\ .$$

If the primary electron is defined as the resulting electron with the highest kinetic energy, then it has a possible range from E' to E'/2, and $\sigma^{T}_{inel}\ (E')$ may also be obtained from

$$\sigma^{T}_{inel}\ (E') = \int_{\frac{E'}{2}}^{E'} dE \int d\Omega\ \frac{d^2\sigma_{inel}\ (E',E,\vec{\Omega}'\cdot\vec{\Omega})}{dEd\Omega}\ .$$

It is this form of $\sigma^{T}_{inel}\ (E')$ that will be used in the text.

for photons,

i = co (Compton scatterings from atomic electrons)

pe (photoelectric absorption, thereby producing an electron),

pp (pair production, thereby producing an electron and a positron);

$\frac{d^2\sigma_{e\to\gamma}(E',E,\vec{\Omega}'\cdot\vec{\Omega})}{dEd\Omega}$ = the differential atomic cross section for an electron with kinetic energy E', going in direction $\vec{\Omega}'$, to produce a photon with kinetic energy E, going in direction $\vec{\Omega}$, by bremsstrahlung scattering;

$\frac{d^2\sigma_{\gamma\to e}(E',E,\vec{\Omega}'\cdot\vec{\Omega})}{dEd\Omega}$ = the differential atomic cross section for a photon with kinetic energy E', going in direction $\vec{\Omega}'$, to produce an electron with kinetic energy E, going in direction $\vec{\Omega}$, by photoelectric absorption or pair production.

Electrons produce photons by bremsstrahlung, and photons produce electrons by photoelectric absorption and pair production. The photon and electron transport equations are therefore cross-coupled and must be solved together. Positron coupling should also be considered since photons produce positrons by pair production and positrons produce photons by bremsstrahlung and annihilation. However, positron transport is not significant for the calculations undertaken here, and so the positron transport equation is not included.

The photon-electron source term in the electron transport equation is small for the transport of incident electrons in the few-MeV range,

and will be neglected here. The electron transport equation is then no longer coupled to the photon transport equation in the photon-electron direction since electrons produced by photons are not included.

The electron transport equation to be solved is

$$\vec{\Omega}\cdot\nabla\phi(\vec{R},E,\vec{\Omega}) = P(\vec{R},E,\vec{\Omega}) + n\int_E^{E_o} dE' \int d\Omega' \frac{d^2\sigma_{e\to e}}{dEd\Omega}(E',E,\vec{\Omega}'\cdot\vec{\Omega})\phi(\vec{R},E',\vec{\Omega}') - n\,\sigma_e^T(E)\phi(\vec{R},E,\vec{\Omega}), \tag{3}$$

which is obtained from Eq. (1) by dropping the photon-electron source term,

$$n\int_E^{E_o} dE' \int d\Omega' \frac{d^2\sigma_{\gamma\to e}}{dEd\Omega}(E',E,\vec{\Omega}'\cdot\vec{\Omega})\phi_\gamma(\vec{R},E',\vec{\Omega}') .$$

Electrons still serve as a source for photons, and an electron-photon transport case will be reported in Section VII. The one-way coupling scheme (electron to photon) is similar to the neutron-photon problem that for some time has been solved by the use of various discrete ordinates codes.

The resulting Eq. (3) for electron transport is solved by the method of discrete ordinates. This method was developed to solve the neutron transport equation analogous to Eq. (3), and electron transport represents a new adaptation. The code used for this adaptation, ANISN[23],

has been notably successful in solving the neutron and photon transport problems. Nevertheless, the cross sections involved for electron transport are so different in form from neutron cross sections that it was not at all clear whether they would be handled correctly. Theoretically, neutrons, photons, or electrons can be transported from an initial angle and energy distribution to a final angular and energy spectrum without a knowledge of the type particle and knowing only the probability of a reaction occurring.

ANISN is able to treat any one-dimensional geometry, but only slab geometry cases are considered here. The exact procedure for obtaining the discrete ordinates form for Eq. (3) is described elsewhere,[24 28] but a brief indication of some of the concepts involved will be presented here for the one-dimensional slab geometry case.

The energy dependence of the flux and the cross sections is expressed in multigroup form. Consider the energy group, G, which extends from E_{g+1} to E_g, where $E_g = E_{g+1} + \Delta E_G$. The electron flux for group G is

$$\phi_G(\vec{R},\vec{\Omega}) = \int_{E_{g+1}}^{E_g} dE\, \phi(E,\vec{R},\vec{\Omega}) \ .$$

The multigroup form of the cross section for an electron with energy E' to produce an electron with energy E is found by integrating the differential cross section over the energy bounds of the initial group

G' from $E_{g'+1}$ to $E_{g'}$ $(E_{g'+1} + \Delta E_{G'})$, and averaging over the initial group and integrating over the energy bounds of the final group, G. Then

$$\sigma_{G'G}(\vec{\Omega}'\cdot\vec{\Omega}) = \frac{d\sigma_{G',G}(\vec{\Omega}'\cdot\vec{\Omega})}{d\Omega} = \frac{\int_{E_{g'+1}}^{E_{g'}} dE' \int_{E_{g+1}}^{E_{g}} dE \; \frac{d^2\sigma_{e\to e}(E',E,\vec{\Omega}'\cdot\vec{\Omega})}{dEd\Omega}}{\Delta E_{G'}} .$$

The angular dependence of the cross sections is expressed in an $(\ell_{max} + 1)$-term Legendre series expansion in μ_o, where μ_o is the cosine of the scattering angle. If the Legendre expansion is defined as

$$n \; \frac{d\sigma_{G',G}(\vec{\Omega}'\cdot\vec{\Omega})}{d\Omega} \simeq \frac{1}{4\pi} \sum_{\ell=0}^{\ell_{max}} M^{\ell}_{G',G} \, L^{\ell}(\mu_o),$$

where $L^{\ell}(\mu_o)$ is the Legendre function, then the series coefficients are given as

$$M^{\ell}_{G',G} = 4\pi\left(\frac{2\ell+1}{2}\right) n \int_{-1}^{+1} d\mu_o \; \frac{d\sigma_{G',G}(\vec{\Omega}'\cdot\vec{\Omega})}{d\Omega} L^{\ell}(\mu_o).$$

The angular variable is then expressed as a function of a fixed-coordinate system in which the angular variable is divided into NOA (number of angles) discrete angular intervals. This is done by use of the addition theorem for Legendre polynomials. The integral over angle in

the Boltzmann equation is replaced by a Gaussian quadrature formula

$$\int d\Omega \phi_G(\vec{\Omega},\vec{R}) = \sum_{D=1}^{NOA} \phi_{G,D}(\vec{R})\omega_D ,$$

where

$$\phi_{G,D}(\vec{R}) = \phi_G(\vec{\Omega}_D,\vec{R}) ,$$

NOA is the total number of points (angles) considered, and $\vec{\Omega}_D$ and ω_D are the ordinates and weights for the Gaussian quadrature. The weights, ω_D, are normalized to give a sum of one instead of 4π, so that for one interval, D,

$$\int_{\Delta\vec{\Omega}_D} d\Omega \; \phi_G(\vec{R},\vec{\Omega}) \simeq \phi_{G,D}(\vec{R})\omega_D$$

with

$$\int_{\Delta\vec{\Omega}_D} d\Omega = 4\pi \; \omega_D \; .$$

The integral over angle in Eq. (3) may then be represented by a summation over the incident angle, D', from D' = 1 to D' = NOA (number of angles). If $\mu = \vec{\Omega} \cdot \vec{k}$, where $\vec{k}$ is the unit vector normal to the slab, then

$$\int_{\Delta\mu_D} \mu\phi_G(\vec{R},\mu)d\mu = \mu_D \; \phi_{G,D}(\vec{R})\omega_D .$$

The spatial region of interest is divided into specific intervals represented by the subscript I,

where

$I = 1$ to number of intervals, and

$r_i =$ the linear distance to the beginning of interval I,

$r_i+1 =$ the linear distance to the end of interval I.

The mean value theorem is then applied to each term in the transport equation giving average flux values for each energy group, spatial interval, and angular interval considered. The resulting discrete ordinates form for Eq. (3) in the one-dimensional multigroup slab geometry form is then

$$\mu_D \left(\phi_{G,i+1,D} - \phi_{G,i,D}\right) = (r_{i+1} - r_i)\, P_{G,I,D}$$

$$+ (r_{i+1} - r_i) \sum_{\ell=0}^{\ell_{max}} A_D^{\ell} \sum_{G'=1}^{G} M_{G',G}^{\ell} \sum_{D'=1}^{NOA} A_{D'}^{\ell}\, \phi_{G',I,D'}\, \omega_{D'} \quad (4)$$

$$- (r_{i+1} - r_i)\, n\, \sigma_G^T\, \phi_{G,I,D} ,$$

where

$\phi_{G,I,D} =$ the electron flux integrated over energy group G, averaged over spatial interval I and evaluated at μ_D in angular interval D,

$\phi_{G,i+1,D} =$ the average electron flux in energy group G and angular interval D at spatial point r_{i+1},

σ_G^T = the total reaction cross section for an electron in group G,

$A_D^\ell = L^\ell(\mu_D)$,

$P_{G,I,D}$ = the external source in a spatial interval I for electrons in energy group G, angular interval D.

The initial Boltzmann equation, Eq. (3), is now represented by a series of equations similar to Eq. (4), with each equation representing the electron balance in a so-called "phase space cell", for which $\phi_{G,I,D}$ (energy group G, spatial interval I, angular interval D) is defined.

The third term in Eq. (4),

$$(r_{i+1}-r_i) \sum_{\ell=0}^{\ell_{max}} A_D^\ell \sum_{G'=1}^{G} M_{G',G}^\ell \sum_{D'=1}^{NOA} A_{D'}^\ell \phi_{G',I,D'} \omega_{D'} ,$$

then represents the number of electrons in energy group G and angular interval D produced in spatial interval I by electrons in all angular intervals (D'=1 to NOA), in all energy groups G' which represent energies greater than or equal to the energies in group G.

In order to solve Eq. (4), it is necessary to evaluate $\phi_{G,I,D}$, $\phi_{G,i+1,D}$, and $\phi_{G,i,D}$. First, it is assumed that the incoming fluxes, $\phi_{G,i,D}$, are known from boundary conditions or from the calculation for the previous interval. Additional difference equations are then assumed in the form

$$\phi_{G,I,D} \simeq a\,\phi_{G,i+1,D} + (1-a)\phi_{G,i,D}, \quad \mu > 0,$$

$$\phi_{G,I,D} \simeq (1-a)\phi_{G,i+1,D} + a\,\phi_{G,i,D}, \quad \mu < 0,$$

where a is determined by a weighted difference model.[29] The discrete ordinates form for the photon transport equation is similar to Eq. (4) with the appropriate photon cross sections used.

As shown in Eq. (4), the discrete ordinates form of the transport equation categorizes the electrons at a particular spatial point in terms of energy groups and angular intervals. The cross sections which transfer electrons from one energy group to another are determined by integrating the differential cross section over the various energy groups, and the angular changes are described by expanding the cross sections in a Legendre series in the cosine of the scattering angle. If the energy and the angular changes are small enough for a particular collision, the incident electron would be in the same energy group and angular interval after the collision as before it. Thus, within the limits of the accuracy of ANISN's calculations, no change has occurred in the energy and angular spectra. Such collisions are very numerous for electrons. An approximation known as the delta-function correction is therefore made in an effort to remove those collisions from the cross sections. The explanation given here is similar to that presented by Mynatt.[26]

Let the within-group Legendre series expansion coefficients be expressed as

$$M^{\ell}_{G,G} = (2\ell+1)\ f_{\ell}, \tag{5}$$

so that the within-group scattering angular distribution, which was given earlier by an $(\ell_{max}+1)$-term Legendre series as

$$n\,\sigma_{G,G}(\mu_o) \simeq \frac{1}{4\pi} \sum_{\ell=0}^{\ell_{max}} M^{\ell}_{G,G}\, L^{\ell}(\mu_o),$$

may now be represented as

$$n\,\sigma_{G,G}(\mu_o) \simeq \frac{1}{4\pi} \sum_{\ell=0}^{\ell_{max}} (2\ell+1) f_{\ell} L^{\ell}(\mu_o) \ . \qquad (6)$$

Because the cross sections are heavily forward peaked, they can be approximated by an ℓ_{max}-term Legendre series plus a delta function in the forward direction:

$$n\,\sigma_{G,G}(\mu_o) \simeq \frac{1}{4\pi} \sum_{\ell=0}^{\ell_{max}-1} (2\ell+1)\, f'_{\ell}\, L^{\ell}(\mu_o) + \frac{1}{4\pi} C\, \delta(\mu_o-1), \qquad (7)$$

where it is assumed that

$$\delta(\mu_o-1) \simeq \frac{1}{2} \sum_{\ell=0}^{\ell_{max}} (2\ell+1) L^{\ell}(\mu_o) \ .$$

The $(\ell_{max}+1)$-term of the within-group expansion coefficients is therefore assumed to be a delta-function coefficient. Since the accuracy of the initial Legendre series representation increases with the number of terms used in the expansion $(\ell_{max}+1)$, the delta-function coefficient assumption should also be a better approximation as ℓ_{max} increases. To determine f'_{ℓ} and C, equate Eqs. (6) and (7), multiply through by a Legendre polynomial $L^{N}(\mu_o)$, where N varies from 0 to ℓ_{max}, and then integrates over μ_o .

Since

$$\sum_{\ell=0}^{\ell_{max}} \int_{-1}^{+1} (2\ell+1)\ f_\ell L^\ell(\mu_o) L^N(\mu_o) d\mu_o$$

$$= 2f_N, \text{ for } N \leq \ell_{max}, \tag{8}$$

$$= 0 \quad \text{for } N > \ell_{max},$$

and

$$\int_{-1}^{+1} C\ \delta(\mu_o - 1) L^N(\mu_o) d\mu_o = C,$$

then it is found that

$$2f'_\ell = 2f_\ell - C \text{ for } \ell \leq \ell_{max}$$

and (9)

$$C = 2f_{\ell_{max}}$$

Multiplying Eq. (9) by $(2\ell+1)$, and combining the result with Eq. (5) gives the equation for the corrected coefficients:

$$M'^{\ell}_{G,G} = M^{\ell}_{G,G} - \left(\frac{2\ell+1}{2\ell_{max}+1}\right) M^{\ell_{max}}_{G,G} . \tag{10}$$

The modified ℓ_{max} - term Legendre series coefficients are used in the scattering integral and the delta function is accounted for by subtracting $f_{\ell_{max}}$ from the total cross section, where

$$f_{\ell_{max}} = \frac{C}{2}$$

$$= \frac{M_{GG}{}^{\ell_{max}}}{2_{\ell_{max}+1}} \quad .$$

The corrected cross-section coefficients are commonly referred to as $P_{\ell_{max}}$-corrected-$P_{\ell_{max}-1}$. The cross sections used in this investigation were P_7-corrected-P_6. (P_ℓ here refers to the Legendre coefficients and is the standard representation. L^ℓ has been used as a matter of convenience). The magnitude of the delta-function correction is quite large for electrons, so that it greatly facilitates the ANISN calculation, especially since the within-group cross section determines the number of iterations required for convergence.

If the required cross sections were known, the solution could now be obtained. With the proper input data, ANISN could be used for obtaining the transmitted electron spectra. However, all the necessary cross sections are not available. The inelastic electron-electron atomic cross sections that are available were derived assuming a collision in which the energy lost by the primary electron is significantly larger than the binding energy of the target electron. Inelastic electron-electron collisions involving a large energy transfer will be referred to as hard collisions. No adequate cross sections are known for collisions involving energy transfers of the order of the binding energy or

smaller. Nevertheless, these cross sections were estimated by Spencer and Fano,[12] and calculations based on a similar estimate have been done as a part of this investigation. Inelastic electron-electron collisions involving a small energy transfer per collision are very frequent for electrons and account for a large part of the total energy degradation. They will be termed "soft collisions."

Inelastic collisions occur so frequently that, as an approximation, electrons can be considered to undergo a continuous slowing down, with a fixed energy loss per unit path length travelled. This quantity is referred to as the stopping power and is well known both experimentally and theoretically.[30] Unfortunately, the needed cross sections cannot be derived from the stopping power alone, since the stopping power represents an integral over the cross section. However, the stopping power is adequate for many applications, and one can account for the energy loss due to soft collisions by utilizing the appropriate stopping power in a continuous slowing-down term. This procedure uses the best information available and has the advantage of avoiding the cross section for low-energy transfer collisions. The continuous slowing-down equation was obtained by the method used by Rossi.[31] A complete derivation can be found in Appendix A, but an outline of the procedure is given here.

Beginning with the electron transport equation, express Eq. (3) as

$$\vec{\Omega}\cdot\nabla\phi(\vec{R},E,\vec{\Omega}) = P(\vec{R}\ E,\vec{\Omega}) + n\int_{E}^{E_o} dE'\int d\Omega'\ \frac{d^2\sigma^*_{e\to e}}{dEd\Omega}\ (E',E,\vec{\Omega}'\cdot\vec{\Omega})\phi(\vec{R},E',\vec{\Omega}')$$

$$+ n\int_{E+I'}^{E_o} dE'\int d\Omega'\ \frac{d^2\sigma_{inel}}{dEd\Omega}\ (E',E,\vec{\Omega}'\cdot\vec{\Omega})\phi(\vec{R},E',\vec{\Omega}') \tag{11}$$

$$- n\,\sigma_1^T(E)\phi(\vec{R},E,\vec{\Omega}) - n\,\sigma_2^T(E)\phi(\vec{R},E,\vec{\Omega}) - n\,\sigma^*_{e\to e}(E)\phi(\vec{R},E,\vec{\Omega})$$

$$+ n\int_{E}^{E+I'} dE'\int d\Omega'\ \frac{d^2\sigma_{inel}}{dEd\Omega}\ (E',E,\vec{\Omega}'\cdot\vec{\Omega})\phi(\vec{R},E',\vec{\Omega})\ ,$$

where

$$\sigma^*_{e\to e} = \sigma_{el} + \sigma_{br}\ ,$$

$$\sigma_1^T\ (E) = \int_{\frac{E}{2}}^{E-I'} dE'\int d\Omega\ \frac{d^2\sigma_{inel}}{dE'd\Omega}\ (E,E',\vec{\Omega}'\cdot\vec{\Omega})\ ,$$

$$\sigma_2^T(E) = \int_{E-I'}^{E} dE'\int d\Omega\ \frac{d^2\sigma_{inel}}{dE'd\Omega}\ (E,E',\vec{\Omega}'\cdot\vec{\Omega})\ ,$$

I' = an arbitrary value taken to be the minimum energy loss allowed in a large energy transfer or hard collision (a collision involving an energy transfer smaller than I' is a soft collision) .

The inelastic scattering terms are now separated into terms describing soft and hard collisions.

Let

$$T = n \int_{E}^{E+I'} dE' \int d\Omega' \; \frac{d^2\sigma_{inel}}{dEd\Omega} (E',E,\vec{\Omega}'\cdot\vec{\Omega})\phi(\vec{R},E',\vec{\Omega}') - n\,\sigma_2^T(E)\phi(\vec{R},E,\vec{\Omega}) \;, \tag{12}$$

where T now describes the scattering due to soft collisions. Now add and subtract

$$n \int_{E}^{E+I} dE' \; \frac{d\sigma_{inel}}{dE} (E',E)\phi(\vec{R}'E',\vec{\Omega})$$

where

$$\frac{d\sigma_{inel}}{dE} (E',E) = \int d\Omega \; \frac{d^2\sigma_{inel}}{dEd\Omega} (E',E,\vec{\Omega}'\cdot\vec{\Omega})$$

$$= \int d\Omega' \; \frac{d^2\sigma_{inel}}{dEd\Omega} (E',E,\vec{\Omega}'\cdot\vec{\Omega}) \;.$$

Assume

$$\frac{d^2\sigma_{inel}\;(E',E,\vec{\Omega}'\cdot\vec{\Omega})}{dEd\Omega} = \frac{d^2\sigma_{inel}\;(E',E)}{dE} \; \frac{\delta(1-\vec{\Omega}'\cdot\vec{\Omega})}{2\pi} \;.$$

That is, the soft collisions involve only an energy degradation and not an angular change. Then

$$T = n \int_{E}^{E+I'} dE' \frac{d\sigma_{inel}(E',E)}{dE} \phi(\vec{R},E',\vec{\Omega})$$

$$- n \int_{E-I'}^{E} dE' \frac{d\sigma_{inel}(E,E')}{dE} \phi(\vec{R},E,\vec{\Omega}) . \tag{13}$$

$\frac{d\sigma_{inel}(E',E)}{dE} \phi(\vec{R},E',\vec{\Omega})$ is now expanded in a Taylor series, and after defining the soft stopping power S(E) to be

$$S(E) = n \int_{E-I'}^{E} dE'(E-E') \frac{d\sigma_{inel}(E,E')}{dE} , \tag{14}$$

it is found that

$$T = \frac{\partial[S(E)\phi(\vec{R},E,\vec{\Omega})]}{\partial E} . \tag{15}$$

Substituting Eq. (15) into Eq. (11) gives the electron transport equation as solved by ANISN with continuous slowing down (AWCS):

$$\vec{\Omega}\cdot\nabla\phi(\vec{R},E,\vec{\Omega}) = P(\vec{R},E,\vec{\Omega}) + n \int_{E}^{E_o} dE' \int d\Omega' \, d^2\sigma^*_{e\to e}(E',E,\vec{\Omega}'\cdot\vec{\Omega})\phi(\vec{R},E',\vec{\Omega}')$$

$$+ n \int_{E+I'}^{E_o} dE' \int d\Omega' \frac{d^2\sigma_{inel}(E',E,\vec{\Omega}'\cdot\vec{\Omega})}{dEd\Omega} \phi(\vec{R},E',\vec{\Omega}') \tag{16}$$

$$- n\,\sigma^*_{e\to e}(E)\phi(\vec{R},E,\vec{\Omega}) - n\,\sigma_1^T(E)\phi(\vec{R},E,\vec{\Omega}) + \frac{\partial}{\partial E}[S(E)\phi(\vec{R},E,\vec{\Omega})] .$$

The difference between Eqs. (3) and (16) is that the inelastic e→e collisions resulting in an energy loss less than I' (the soft collisions) are now handled by a continuous slowing-down term. The soft collisions are treated as part of the inelastic and total removal cross sections in Eq. (3), although the cross sections for the soft collisions are not well known. In Eq. (16), the energy loss due to these soft collisions is treated by a continuous slowing-down term. The stopping power used in the continuous slowing-down term is not the well-known energy loss per unit distance due to excitation and ionization but a portion of it, and will be described in detail in the next section. No knock-on electrons are produced from soft collisions treated by Eq. (16), and the incident electron involved suffers an energy degredation, but no angular deflection. To obtain the discrete ordinates form for T [Eq. (15)], integrate over the energy bounds of group G. Then

$$\int_{E_{g+1}}^{E_g} \left(\frac{\partial[S(E)\phi(\vec{R},E,\vec{\Omega})]}{\partial E}\right) dE = S(E_g)\phi(\vec{R},E_g,\vec{\Omega}) - S(E_{g+1})\phi(\vec{R},E_{g+1},\vec{\Omega}), \qquad (17)$$

which is then incorporated into Eq. (16) to give

$$\mu_D(\phi_{G,i+1,D} - \phi_{G,i,D}) = (r_{i+1} - r_i)P_{G,I,D} + (r_{i+1} - r_i) \sum_{\ell=0}^{\ell_{max}} A_D^{\ell} \sum_{G'=1}^{G}$$

$$\times M^{*\ell}_{G',G} \sum_{D'=1}^{NOA} A^{\ell}_{D'} \phi_{G',I,D'} \omega_{D'} - (r_{i+1} - r_i) n \, \sigma^{*T}_{G,I} \phi_{G,I,D} \quad (18)$$

$$+ (r_{i+1} - r_i) [S_{g,I} \phi_{g,I,D} - S_{g+1,I} \phi_{g+1,I,D}] .$$

In Eq. (18),

$\phi_{g,I,D}$ = the average electron flux in spatial interval I, evaluated at μ_o in angular interval D with energy E_g,

$S_{g',I}$ = the stopping power (energy loss/cm) due to soft collisions for electrons in interval I with energy E_g,

$$\sigma^{*T}(E) = \sigma^{*}_{e\to e}(E) + \sigma^{T}_{1}(E),$$

$$= \sigma_{el}(E) + \sigma_{br}(E) + \sigma^{T}_{1}(E),$$

$$M^{*\ell}_{G',G} = 4\pi \left[\frac{2\ell+1}{2}\right] n \int_{-1}^{+1} \sigma^{*}_{G'\to G,I}(\vec{\Omega}'\cdot\vec{\Omega}) \, L^{\ell}(\mu_o) \, d\mu_o$$

= ℓth Legendre expansion term for the e→e scattering due to elastic, bremsstrahlung and hard inelastic collisions.

$\phi_{g,I,D'}$ $\phi_{g+1,I,D'}$ and $\phi_{G,I,D}$ are interrelated by a weighted difference model[29] similar to that used for spatial intervals.

IV. TRANSPORT CROSS-SECTION DATA

Described in this section are the cross sections and other parameters used in the electron and photon transport calculations presented in Sections V, VI, and VII.

Electrons with kinetic energies below 10 MeV undergo three significant reactions:[5] inelastic scattering from atomic electrons, elastic or Coulomb scattering from atomic nuclei, and bremsstrahlung (radiative) interactions with both atomic electrons and nuclei.

A. Inelastic Electronic Scattering from Atomic Electrons

Møller[5,17] derived a relativistic cross section for an inelastic electronic collision with a free electron at rest, which may be stated as

$$\frac{d\sigma_M(E',E)}{dE} = \frac{2\pi r_0^2 \psi Z}{E'^2} \left\{ \frac{1}{(E/E')^2} + \frac{1}{(1-E/E')^2} - \frac{2K-1}{K^2} \times \frac{1}{(E/E')(1-E/E')} + \frac{K-1}{K} \right\}^2 , \tag{19}$$

where

$$\frac{d\sigma_M(E',E,\vec{\Omega}'\cdot\vec{\Omega})}{dE\,d\Omega} = \frac{d\sigma_M(E',E)}{dE} \times \frac{\delta[\cos\theta - f(E',E)]}{2\pi}$$

since in a two-body collision the scattering angle is a function of the initial and final energy of the particle considered;

E' = the initial kinetic energy of the incident electron;

E = the final kinetic energy of the primary electron;

$E'-E$ = the kinetic energy lost by the primary electron in the collision, which is also the kinetic energy of the secondary electron produced by the collision;

Z = the atomic number of the target atom;*

$K = (E'+m)/m$;

m = the electron rest mass;

r_o = the classical electron radius;

$\psi = m/\beta^2$;

β = the ratio of the velocity of the incident electron to the velocity of light;

$$f(E',E) = \cos\theta_h, \quad E \geq E'/2;$$
$$= \cos\theta_\ell, \quad E < E'/2.$$

The resultant electron with the highest kinetic energy is defined as the primary electron. The maximum energy transfer per collision is therefore $E'/2$. The angle of scattering θ_ℓ of the electron emerging with the lower energy (secondary or knock-on electron) is given by[5]

*The cross section given here is not the normal Møller formula but Z × Møller cross section for an electron-electron collision, since the atomic form is used in this investigation.

$$\theta_\ell = \left[\frac{(E'-E)(E'+2m)}{(E'-E)E'+2m}\right]^{\frac{1}{2}} , \tag{20}$$

and θ_h for the primary electron by

$$\theta_h = \left[\frac{E(E'+2m)}{EE'+2m}\right]^{\frac{1}{2}} , \tag{21}$$

where $\cos\theta_h \geq \cos\theta_\ell \geq 0$.

If the energy transferred by the incident electron to the atomic electron is large enough so that the binding energy is insignificant (hard collision), the atomic electron can be assumed to be free, and the Møller cross section is applicable. When the energy transfer is of the order of the binding energy, the collision does not fit the Møller cross-section criteria. One approach used in this investigation to treat such collisions was based on the work of Spencer and Fano.[12] This method assumes that for inelastic electron-electron collisions involving a small energy transfer, only the rate of energy dissipation is important. The procedure used to determine the energy loss per unit pathlength is similar to that formulated by Rohrlich and Carlson.[9] From Eq. (14), the stopping power for the low-energy transfer (soft) collisions is

$$S(E') = n \int_{E'-I'}^{E'} dE\ (E'-E)\ \frac{d\sigma_{inel}(E',E)}{dE} .$$

The Bethe[9,32] theory of stopping power, in which an explicit summation is conducted over the excitation probabilities of the atom, predicts that for low-energy transfer collisions

$$S(E') = n_e(2\pi r_o^2\psi) \left\{ \ln \left[\frac{2E'I'(K+1)}{I^2} \right] - \beta^2 - \delta^* \right\}, \tag{22}$$

where

n_e = the electronic number density of the target material;

δ^* = the Sternheimer[33] correction for the density effect, the mean-energy-loss reduction due to polarization of the medium;

I = the average ionization energy for the target material;

I' = the minimum energy transfer for a hard (high-energy transfer) collision.

Analagous to Eq. (14), the stopping power for hard collisions may be expressed as

$$S_{hard}(E') = n \int_{E'/2}^{E'-I'} dE(E'-E) \frac{d\sigma_M(E',E)}{dE} . \tag{23}$$

Direct integration yields

$$S_{hard}(E') = n_e(2\pi r_o^2\psi) \left\{ \ln\left(\frac{E'}{2I'}\right) + \ln\left[\frac{E'}{2(E-I')}\right] + 2 - \frac{E'}{E'-I'} \right.$$
$$\left. + \left(\frac{K-1}{K}\right)^2 \left(\frac{1}{8} - \frac{I'^2}{2E'^2}\right) + \left(\frac{2K-1}{K^2}\right) \ln\left[\frac{E'}{2(E'-I')}\right] \right\} . \tag{24}$$

From Eqs. (22) and (24), the total energy loss per unit pathlength due to inelastic electronic collisions with atomic electrons is

$$S_{total}(E') = n_e(2\pi r_o^2\psi) \left\{ \ln \left[\frac{E'(K+1)}{2I^2(E'-I')} \right] + 2 - \frac{E'}{E'-I'} \right.$$

$$\left. + \left(\frac{K-1}{K}\right)^2 \left(\frac{1}{8} - \frac{I'^2}{2E'^2}\right) + \left(\frac{2K-1}{K^2}\right) \ln \left[\frac{E'}{2(E'-I')}\right] - \beta^2 - \delta^* \right\} . \tag{25}$$

Eq. (25) differs from the result of the Rohrlich and Carlson derivation by the presence of smaller terms (no assumption was made as to the relative sizes of E' and I') and the inclusion of the Sternheimer[33] correction. Spencer and Fano defined a minimum energy loss per collision so that the correct stopping power, here given by Eq. (25), is obtained by the use of the Møller cross section. The definition may be expressed as

$$S_{total}(E') = n \int_{\frac{E'}{2}}^{E'-I'} dE(E'-E) \frac{d\sigma_M(E',E)}{dE} ,$$

$$= S_{hard}(E') . \tag{26}$$

Since I' here is the minimum energy loss allowed in any collision, there is no separate soft energy loss term. I' is now a function of E'. Setting S_{total} [Eq. (25)] equal to S_{hard} [Eq. (24)] and solving for I' gives

$$I' = \frac{I^2 \exp(\beta^2+\delta)}{2(K+1)E'} \tag{27}$$

as the minimum energy loss per inelastic collision with an atomic electron for an incident electron with kinetic energy E'. The I' values obtained from Eq. (27) are approximately four orders of magnitude smaller than I and therefore far below the energy loss range for which the Møller cross sections were derived. However, in the absence of an adequate differential cross section for soft collisions, the use of the Møller cross section down to I' in Eq. (3) does guarantee the correct stopping power. This should be sufficient if the form of the cross section is unimportant for soft collisions and only the energy loss matters, as Spencer and Fano assumed. This type of calculation will be referred to as ANISN with the Møller cross section used to treat low-energy transfer collisions (AWMC). A typical first within-group cross-section expansion coefficient, (P_o term of $\Sigma_{G\to G}$), is of the order of 10^6 before correction, but of the order of 10^2 after the delta-function correction.

As an alternate treatment, these lower energy transfer (soft) collisions were approximated by a continuous slowing-down term,

$$\frac{\partial S(E)\phi(\vec{R},E,\vec{\Omega})}{\partial E} ,$$

in Eq. (16). The stopping power for soft collisions, S(E), is defined by Eq. (22) as

$$S(E) = n_e(2\pi r_o^2\psi) \left\{ \ln \left[\frac{2EI'(K+1)}{I^2} \right] - \beta^2 - \delta^* \right\} .$$

The only undetermined parameter in the S(E) definition is I', the minimum energy transfer for a hard collision. It is not at all clear what value should be used. I' must be high enough for the Møller cross sections to be valid. On the other hand, too high a value would have undesirable effects on the angular distribution and electron population since the continuous slowing-down approximation assumes collisions are straightahead and does not account for secondary electrons. In general, it seems reasonable to assume that I' should be greater than I, the average ionization energy. The use of the continuous slowing-down approximation to handle low-energy transfer collisions does have some advantages as a method for calculating electron transport. The correct total stopping power is assured when the hard energy loss obtained in Eq. (23) is combined with the soft energy loss from Eq. (22). Also, the continuous slowing-down approximation alleviates the need for a soft-collision cross section by assuming a uniform, continuous energy loss involving no change of direction. This type of calculation will be referred to as ANISN with continuous slowing-down used to treat low-energy transfer collisions (AWCS). A typical first within-group cross-section expansion coefficient is of the order of 10^4 before correction, but of the order of 10^2 after the delta-function correction.

B. Elastic Coulomb Scattering from Atomic Nuclei

The differential cross section used here for elastic scattering from a nucleus is based on the Mott[5,34] series (evaluated as the ratio of Mott-to-Rutherford cross sections[34]), with the Molière[7] screening angle and Spencer's[35] treatment for low-angle scattering. Goudsmit and Saunderson's[5,8] expression for the screened Rutherford cross section with Molière's[7] screening angle is

$$\frac{d\sigma(E,\vec{\Omega}'\cdot\vec{\Omega})}{d\Omega} = \left[\frac{2\pi e^4 F(Z)}{p^2 v^2} \times \frac{\sin\theta\, d\theta}{(1-\cos\theta + \frac{1}{2}\,\theta_s^2)^2}\right] \times R\ , \qquad (28)$$

where

θ_s = Molière's[7] screening angle that attempts to account for the screening of the nuclear potential by atomic electrons;

$F(Z) = Z^2$ for nuclear scattering;

e = the electron charge;

p = the relativistic momentum of the incident electron;

v = the relativistic velocity of the incident electron;

R = the ratio of Mott-to-Rutherford* scattering cross sections.

Spencer[36] rearranged the cross section in Eq. (28) to get a better expression for small scattering angles and obtained

*Since the Mott series is infinite, the Mott-to-Rutherford ratio can be represented only by an infinite series. The series representation was not given here because it is too complicated, but a full discussion can be found in Doggett and Spencer's article.[35]

$$\frac{d\sigma(E,\vec{\Omega}.\vec{\Omega})}{d\Omega} = \left[\frac{2\pi e^4 F(Z)}{p^2 v^2} \times \frac{\sin\theta \, d\theta}{(1-\cos\theta + \frac{1}{2}\,\theta_s^2)^2} \right]$$

$$\times \left\{ [1 + \frac{\pi}{\sqrt{2}} (\frac{Z}{137})\beta \cos\psi](1-\cos\theta + \frac{1}{2}\,\theta_s^2)^{\frac{1}{2}} + [R-1- \frac{\pi}{\sqrt{2}} \right. \tag{29}$$

$$\left. \times (\frac{Z}{137})\beta \cos\psi(1-\cos\theta)^{\frac{1}{2}}] \left[\frac{1-\cos\theta + \frac{1}{2}\,\theta_s^2}{1-\cos\theta} \right]^2 \right\} ,$$

where

$$\cos\psi = R_e \left[\frac{\Gamma\left(\frac{1}{2} - i\,\frac{Z}{137\beta}\right) \Gamma\left(1 + i\,\frac{Z}{137\beta}\right)}{\Gamma\left(\frac{1}{2} + i\,\frac{Z}{137\beta}\right) \Gamma\left(1 - i\,\frac{Z}{137\beta}\right)} \right] .$$

C. <u>Bremsstrahlung (Radiative) Interactions with Nuclei and Atomic Electrons</u>

The differential cross section used to describe bremsstrahlung interactions is given by McCormick, Keiffer, and Parzen,[37] who recalculated the work of Racah,[38] as

$$\frac{d\sigma(E',E,\vec{\Omega}'.\vec{\Omega})}{dEd\Omega} = \frac{1}{2\pi} \times \frac{Z^2}{137} \left(\frac{e^2}{m}\right)^2 \frac{p}{p'} \frac{1}{k} \times C \times F , \tag{30}$$

where

p = the relativistic final momentum of the electron;

p' = the incident momentum of the electron;

k = the energy of the emitted photon;

C = a dimensionless parameter, defined in Ref. 35, which is a function of the initial and final electron energies;

F = a high-frequency limit correction factor, defined as

$$= \frac{X}{1-e^{-X}}, \qquad p \neq 0;$$

$$= X, \qquad p = 0;$$

where $X = \frac{2\pi ZE}{137p}$.

The high-frequency end-point correction is necessary so that, after integration over angle, the cross section will not approach 0 as the kinetic energy of the electron after the collision approaches 0. Koch and Motz[16] present Fano's formula for the high-frequency limit cross section. The derivation of the correction factor used here is presented in Appendix B. It should be noted that this correction is only very approximate since it is designed to give the correct limit after integration over angle. There is no indication of the effect of the correction at a specific angle. Eq. (30) exhibits the well-known $\frac{1}{K}$ divergence when $E'=E(K=0)$, so the energy integral over the differential bremsstrahlung cross section was cut off at $E'=E-10^{-4}$. Therefore, collisions that involve an electron energy loss of $<10^{-4}$ MeV and photon production with a maximum energy $<10^{-4}$ MeV are not considered.

D. Photon Interactions

The photon cross sections used in the solution of the electron-photon case presented in Section VII were taken from a photon cross-section library tape prepared by MUG.[39] The Klein-Nishina approximation[40] for unpolarized photon scattering from free electrons at rest was used to account for Compton scattering. The photoelectric and pair-production cross sections were obtained from data evaluated by McMaster et al.[41] and by Plechaty and Terrall.[42]

V. COMPARISON WITH THEORETICAL MODELS

A. Elastic Multiple-Scattering Angular Distribution

Goudsmit and Saunderson[8] obtained an analytic expression for the angular distribution of transmitted electrons when monoenergetic electrons are normally incident on a sufficiently thin slab so that the energy degradation of the electrons may be neglected. Berger[18] used the Goudsmit-Saunderson theory to obtain the angular distribution of the transmitted electrons resulting from 1-MeV electrons normally incident on an aluminum slab of thickness 0.0287 g/cm^2. The Mott[33] elastic scattering cross section, modified to account for the screening of the nuclear charge by the orbital electrons, was used in the expansion. The transmitted angular current of electrons calculated by Berger is represented by the histogram shown in Fig. 1. The ANISN results for this case are given as the plotted points. In the ANISN calculation, one energy group with a range from 1.0106 MeV to 0.9894 MeV and a midpoint of 1.0 MeV was used. No energy degradation was allowed and only elastic scattering was permitted; i.e., in this calculation Eq. (3) was solved with $\sigma_{inel} = \sigma_{br} = 0$.

The two calculations shown in Fig. 1 are in excellent agreement, and thus the method of discrete ordinates can handle small-angle multiple Coulomb scattering successfully.

B. Inelastic-Scattering Energy Distribution

An analytic solution to the electron transport problem is reported by Passow[43] and by Alsmiller[44] for a particular form of the scattering cross section in which the straightahead approximation is

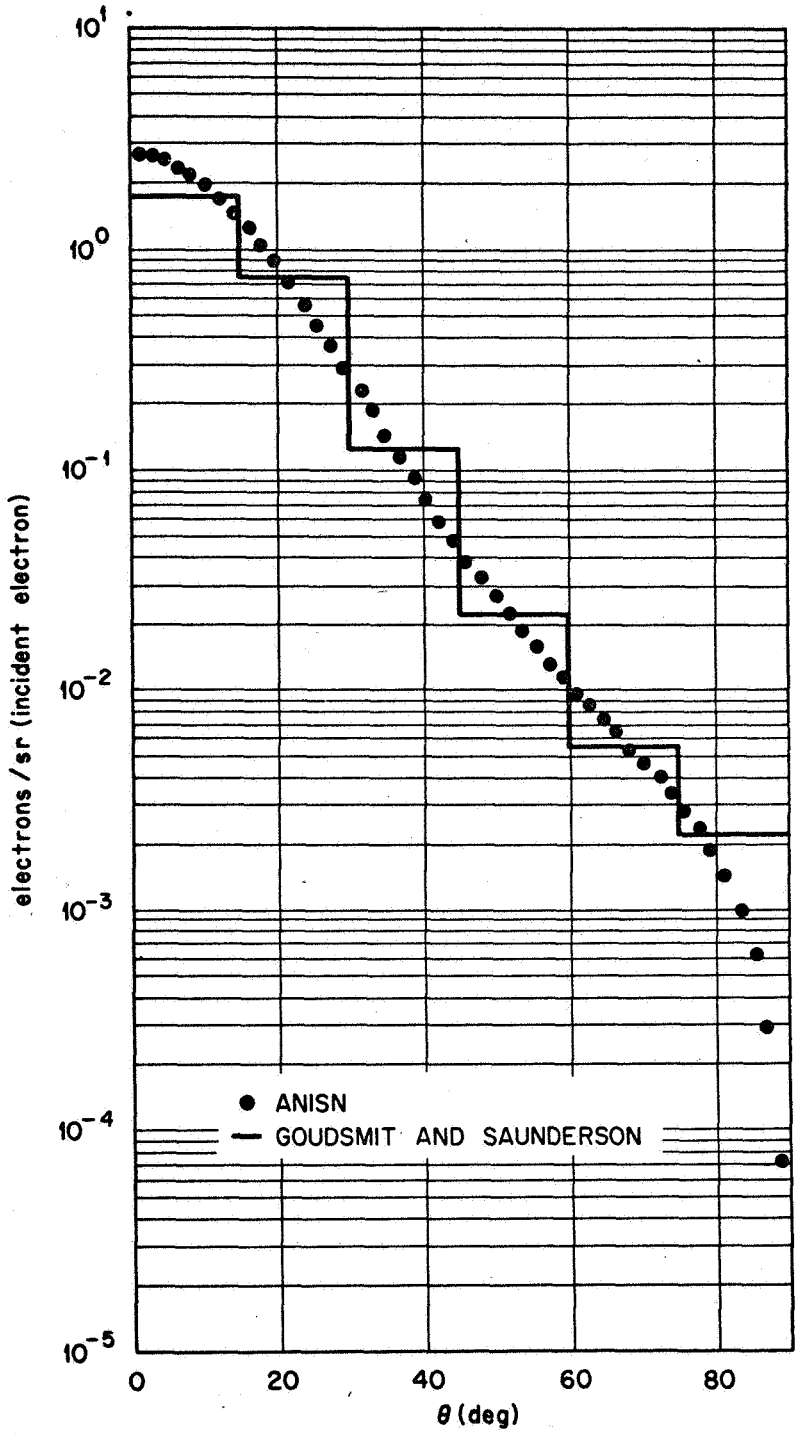

Fig. 1. Angular distribution of transmitted electron current for 1-MeV electrons normally incident on a 0.0287-g/cm^2-thick aluminum slab.

assumed so that there are no angular effects. The source for mono-energetic incident electrons of kinetic energy E_o is expressed as

$$\phi(E,0) = N_o\ \delta(E_o-E)\ ,$$

where

N_o = the source strength, taken as 1.0 in the calculations reported here.

The flux at distance r is

$$\phi(E,r) = N_o\ \delta(E_o-E)e^{-Qr}+\phi_s(E,r)\ , \tag{31}$$

where

Q = the total cross section, which has a constant value for all energies;

$\phi_s(E,r)$ = the secondary electron flux.

The solution for the secondary electron flux is

$$\phi_s(E,r) = Qe^{-Qr}F_{ee}(E',E)N_o g(E_o)\left[\frac{r}{B(E_o,E)}\right]^{\frac{1}{2}} \times I_1\left[2\sqrt{rB(E_o,E)}\right]\ , \tag{32}$$

where

$F_{ee}(E',E)$ = the number per unit energy of electrons with energy E produced in a nonelastic collision of an electron with energy E',

$$= \frac{(2-m)}{E'} \times \left(\frac{E'}{E}\right)^m\ ;$$

m = an input parameter;

$$g(E_o) = E_o^{(m-1)} \;;$$

$$B(E_o,E) = Q \int_E^{E_o} \frac{(2-m)}{\bar{E}}\, d\bar{E} \;;$$

I_1 = the modified Bessel function of the first kind.[45]

The differential inelastic cross section used in the analytic calculation is

$$\frac{d\sigma_{AN}(E',E)}{dEd\Omega} = \sigma Z F_{ee}(E',E)\, \frac{\delta(1-\cos\theta)}{2\pi} \;, \tag{33}$$

where

$\sigma = \frac{Q}{n}$, the total microscopic cross section.

A set of comparisons was made with this analytic solution in order to verify ANISN's ability to calculate the energy distribution resulting from inelastic collisions. Since the inelastic cross section is proportional to $(E'/E)^m$, a small, positive m allows downscatter over a considerable range of E values, while a large, negative m severely restricts the E values from a given E'. It was therefore possible to simulate inelastic collisions resulting in a large energy transfer and those resulting in a small energy transfer. With a known solution and known cross sections, any discrepancy between the analytic results and ANISN's calculations must be due to ANISN's method of solution.

Equation (3) was solved with $\sigma_{br} = \sigma_{el} = 0$, and σ_{inel} was replaced with σ_{AN} from Eq. (33), except that

$$\nu_{AN}\sigma^{T}{}_{AN}(E) = \int_0^E dE' \int d\Omega \frac{d^2\sigma_{AN}(E,E')}{dE'd\Omega}$$

where $\sigma^{T}{}_{AN} = \sigma$, a constant, and the multiplicity

$$\nu_{AN} = \int_0^E dE'F(E',E),$$

because the analytic cross section is not symmetric about $\frac{E}{2}$.

It should be noted, however, that the cross section form given in Eq. (33) is only a very rough approximation to the Møller cross section given in Eq. (19). It is difficult, therefore, to predict ANISN's ability to handle the Møller cross section on the basis of the analytic results presented here. Figure 2 shows the differential cross section at $E' = 1$ MeV, $0 \le E \le 1$ MeV, for the analytic cases considered and for the Møller formula. Since the Møller cross section diverges as $E \to E'$ and is symmetric about $E = E'/2$, the primary electron from a Møller collision is considered to have a kinetic energy E, where $E'/2 \le E \le E'-I'$, and the secondary electron has a kinetic energy of $E'-E$. The total microscopic Møller cross section for a 1-MeV incident electron in aluminum is 2.18×10^2 barns for $I' = 100\ I$ (1.63×10^{-2} MeV), 2.29×10^4 barns for $I' = I$ (1.63×10^{-4} MeV), and 3.53×10^8 barns when I' is determined by the Spencer-Fano procedure (1.07×10^{-8} MeV).

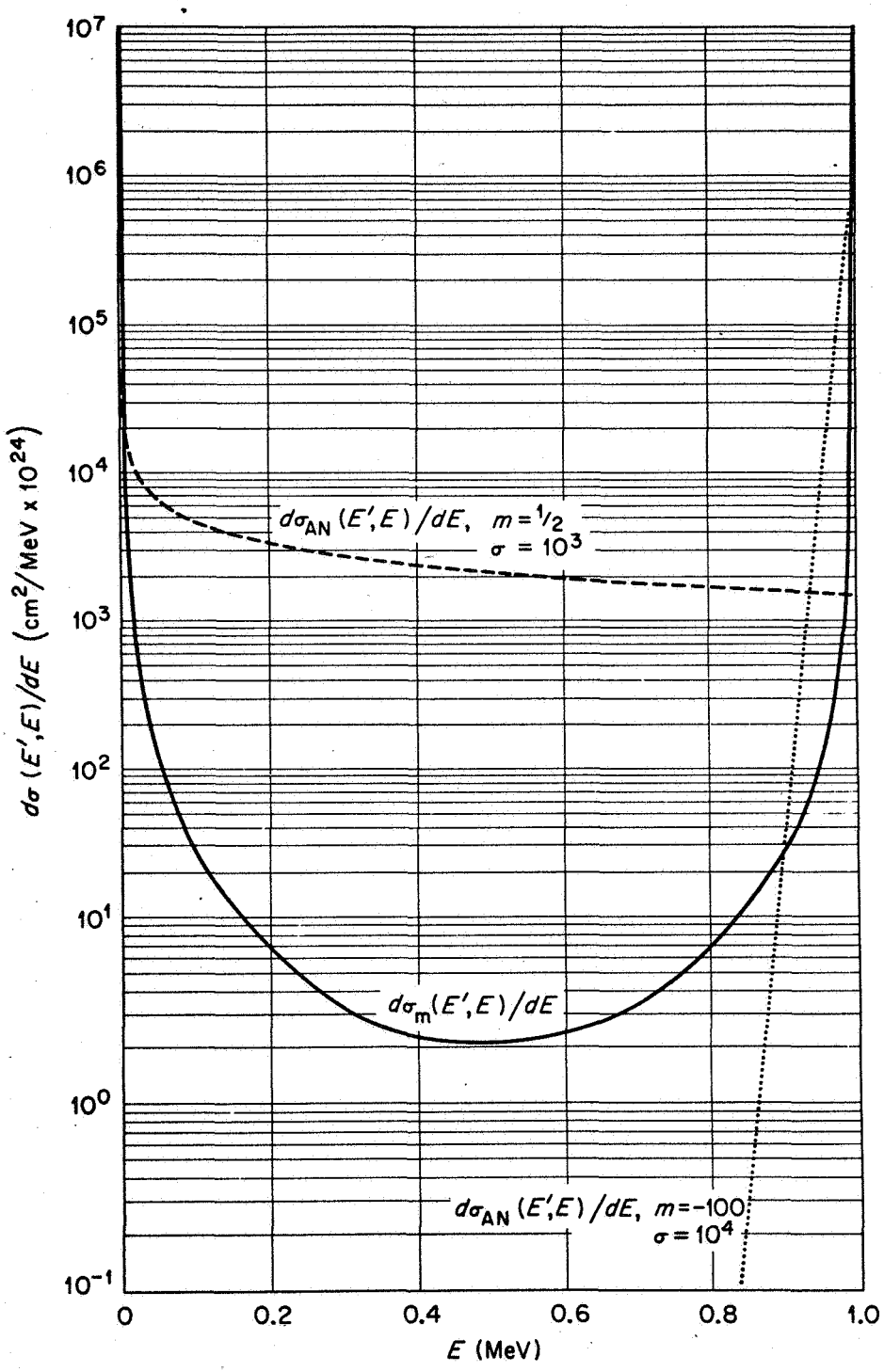

Fig. 2. Comparison of the differential Møller cross section for inelastic electron-electron collisions with two differential analytic cross sections below 1 MeV.

Two separate analytic cases were run, both for 1-MeV electrons normally incident on aluminum slabs, so that $E_o = 1.0$ MeV and $Q = 0.0602252 \times \sigma$. The first case set $m = 1/2$ and $\sigma = 10^3$. Figure 2 shows that the analytic differential cross section for this case very slowly increases from a value of 1.5×10^3 barns/MeV at E = 1 MeV to 4.7×10^3 barns/MeV at E = 0.1 MeV. By comparison, the Møller cross section is much larger near E = 1 MeV but much lower from E = 0.9 MeV to E = 0.5 MeV. With a total microscopic cross section of 10^3 barns, this analytic case has more large energy-transfer collisions, over a wide range of possible transfers, than does the Møller cross section. The ANISN calculation used 40 energy groups from 1.0 MeV to 0.1 MeV. In Fig. 3, results are plotted for aluminum slabs 0.11 g/cm^2 thick and 0.33 g/cm^2 thick. Both plots show extremely close agreement between the analytic solution and ANISN's calculated values. This indicates that the method of discrete ordinates can successfully be used to calculate the results of inelastic scattering over a wide energy range for the specific cross-section form given here. The small high-energy peaks appearing in Fig. 3 represent the uncollided current, expressed as $N_o\ \delta(E-E)\ e^{-Qr}$ for the analytic case in Eq. (31), and the electron current remaining in the source group for ANISN.

The second analytic case set $\sigma=10^4$ and $m = -100$. As can be seen from Fig. 2, this results in a large differential cross section for small energy-transfer collisions, with relatively few collisions below E = 0.9 MeV. However, this analytic differential cross section has a

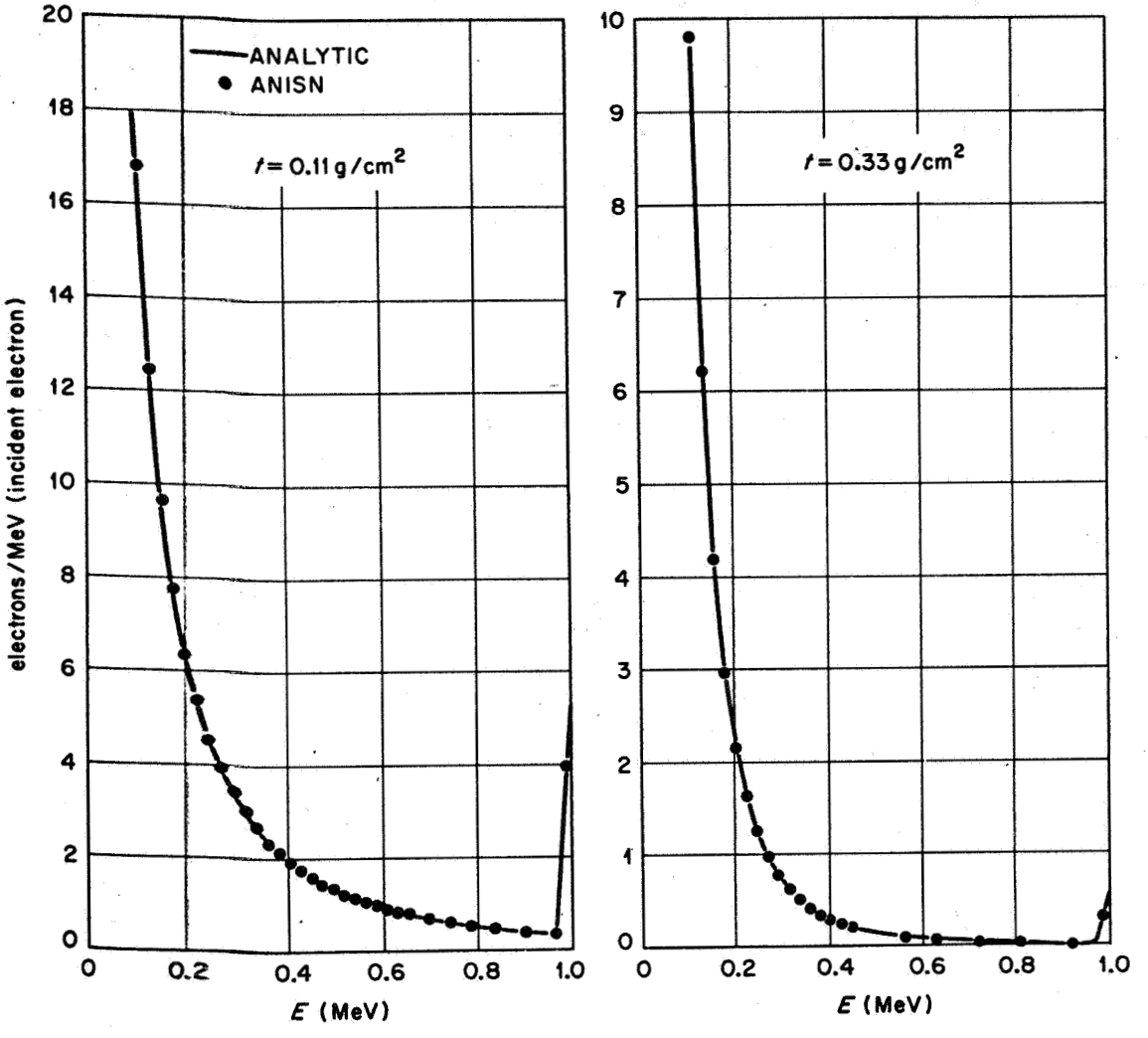

Fig. 3. Transmitted electron current per unit energy per incident electron for 1-MeV electrons normally incident on 0.11-g/cm^2-thick and 0.33-g/cm^2-thick aluminum slabs.

finite value of 1.02×10^6 barns/MeV at E = 1 MeV, while the Møller differential cross section diverges as $E \rightarrow 1$ MeV. The Møller cross section then results in a great number of very small energy-transfer collisions that are not present in this analytic case. The total microscopic cross section, 10^4 barns, roughly corresponds to that obtained from the Møller cross section with $I' = I = 1.63 \times 10^{-4}$ MeV (2.12×10^4 barns), but it is much smaller than in the case where $I' = 1.07 \times 10^{-8}$ MeV (3.53×10^8 barns). The target was a 0.66 - g/cm^2 - thick aluminum slab, and results were obtained for several depths within the slab. In Fig. 4 the analytic transmitted energy spectra are plotted along with ANISN's solution for 0.11 g/cm^2, 0.33 g/cm^2, and 0.66 g/cm^2 thicknesses. In the ANISN calculation 80 energy groups from 1.0 MeV to 0.1 MeV are used. Agreement between the analytic solution and ANISN's calculation is reasonable for all three thicknesses, indicating that the transmitted energy spectrum obtained from this particular cross section can be correctly calculated using the method of discrete ordinates. It should be noted that a large number of smaller-energy-transfer collisions results in a transmitted spectrum in the form of a thin spike, somewhat like a delta function distribution.

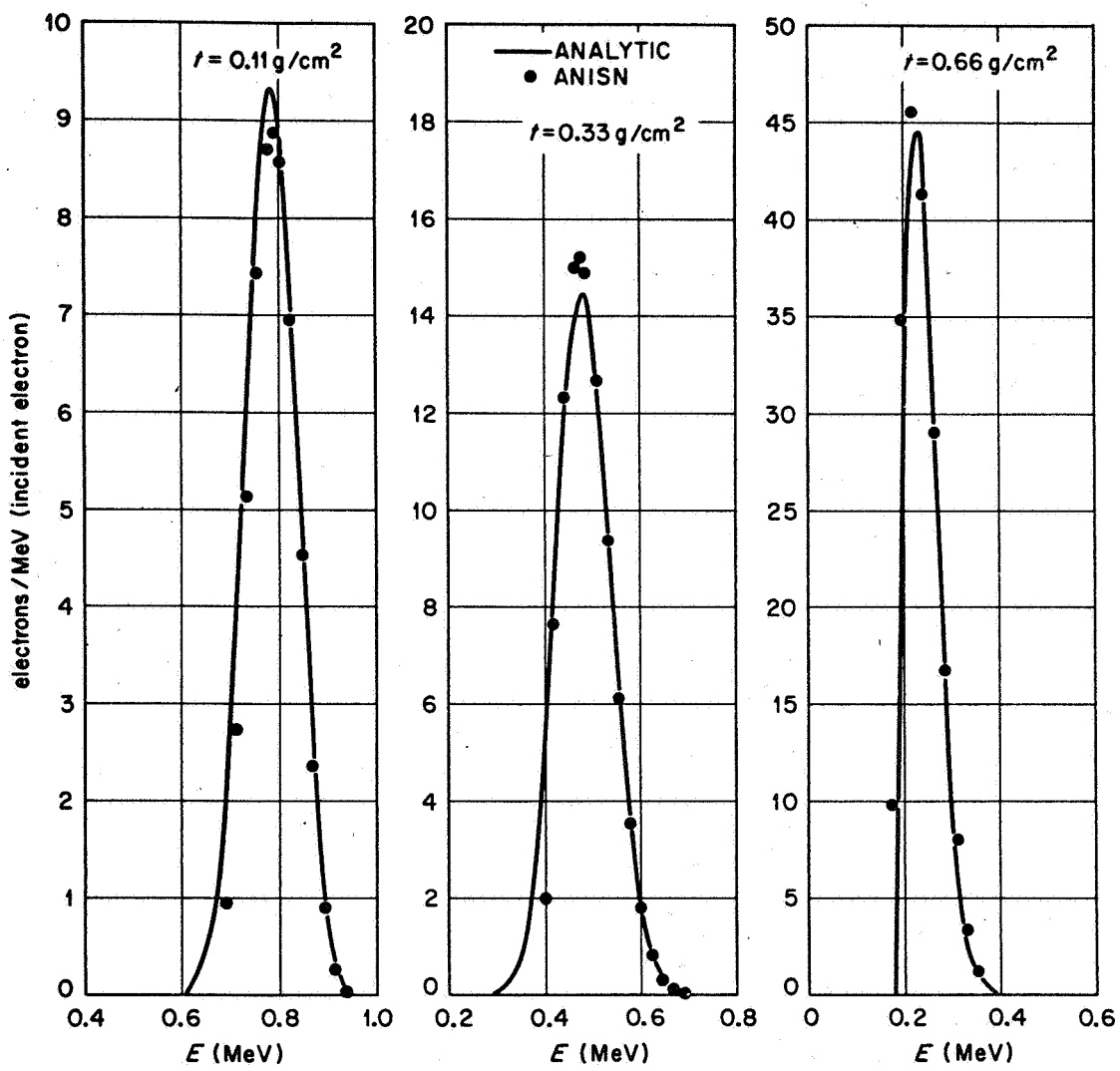

Fig. 4. Transmitted electron current per unit energy per incident electron for 1-MeV electrons normally incident on 0.11-g/cm^2-, 0.33-g/cm^2-, and 0.66-g/cm^2-thick aluminum slabs.

VI. COMPARISON WITH EXPERIMENTAL RESULTS

In this section the transmitted current of electrons calculated by the method of discrete ordinates is presented, along with the experimentally measured spectra for cases involving monoenergetic electrons normally incident on target slabs of varying thicknesses. Calculational results from the Monte Carlo code ETRAN[3] where available in suitable form are also included for additional comparison.

A. Experiments of Rester

The experimental data presented here are taken from the work of Rester[46] and Rester and Derrickson.[47] The Monte Carlo spectra were calculated using ETRAN-15. Results are given for normal incidence of 1-MeV electrons on Al and Au targets and for 2.5-MeV electrons on Al targets.

1. 1-MeV Electrons Incident on Aluminum

The points plotted in Fig. 5 show the measured transmitted electron current per unit energy for 1-MeV electrons normally incident on aluminum slabs of thicknesses of 0.10 g/cm^2, 0.22 g/cm^2, and 0.32 g/cm^2, respectively, roughly corresponding to 0.2, 0.4, and 0.6, respectively, of the range of the incident electron. The solid curves in the figure represent the results from the discrete ordinates calculations using a continuous slowing-down term with I' = 10I to treat soft inelastic collisions, designated by AWCS (ANISN with continuous slowing down), and the dashed curves represent the results from the discrete ordinates calculations using the Møller cross section

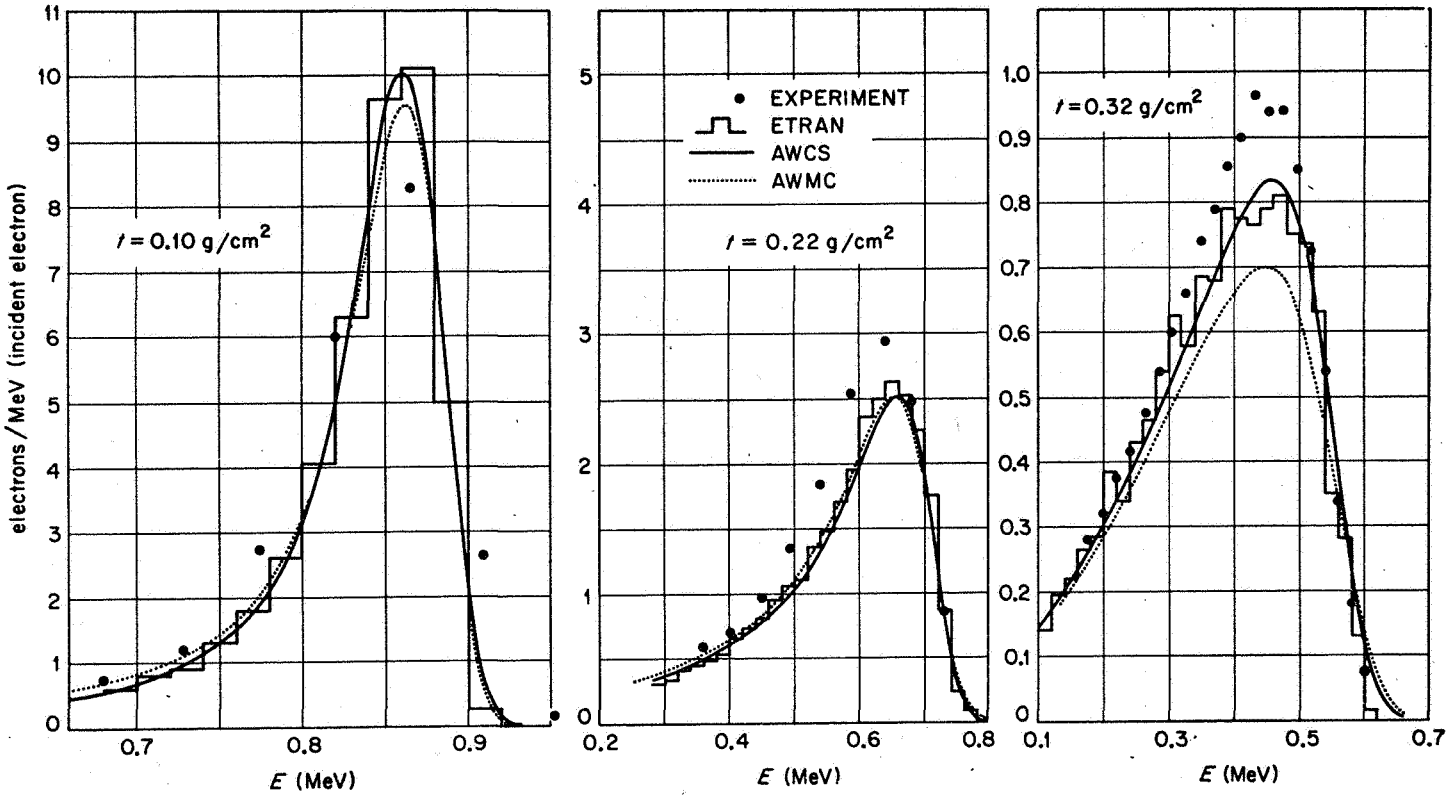

Fig. 5. Transmitted electron current per unit energy per incident electron for 1-MeV electrons normally incident on 0.10-g/cm^2-, 0.22-g/cm^2-, and 0.32-g/cm^2-thick aluminum slabs.

to deal with soft inelastic collisions, designated by AWMC (ANISN with Møller cross section). The solid histograms represent the Monte Carlo calculations. For the 0.10-g/cm^2 case, the experimental results are lower than the calculated results at the peak of the distribution, but they are greater elsewhere, especially at the higher energies. In the 0.22-g/cm^2 and 0.32-g/cm^2 cases, however, agreement between experimental results and theoretical calculations are better along the high-energy edge of the distribution than at the peak or lower energy edge. In general, the results of the discrete ordinates calculations are in reasonably good agreement with those of the experimental measurements. It should be noted, however, that the results of the discrete ordinates and Monte Carlo calculations appear to be in better agreement with each other than with the experimental measurements. The AWCS results are somewhat higher than the AWMC results and for the 0.10-g/cm^2 and 0.32-g/cm^2 cases, are in particularly good agreement with the Monte Carlo calculations.

Since the discrete ordinates approximation approaches the Boltzmann transport equation as the number of energy groups and spatial intervals are increased, the accuracy of the calculation is dependent on these parameters. In general, for the discrete ordinates calculations undertaken in this investigation, an increase in the number of energy groups used to describe a case causes the resulting spectrum to become more sharply peaked and to shift the peak of the spectrum to a slightly higher energy. Increasing the number of spatial intervals tends to decrease the magnitude of the transmitted spectrum. Both of these effects continue up to a point, beyond which no change is noted

in the transmitted spectrum as a result of an increase in the number of spatial intervals or energy groups. Unless otherwise stated, the results presented in this investigation are considered to be converged. The number of energy groups and spatial intervals utilized in a particular calculation is limited by the core storage capacity of the computer and by the time required for the computation. Various calculations were made for the case of 1-MeV electrons normally incident on a 0.22-g/cm^2 thick aluminum slab in order to make a direct comparison between the two discrete ordinates calculational methods and to show the effects of some factors. Two AWCS calculations were made, one with $I' = 10I$ using 160 energy groups and 100 spatial intervals and another with $I' = 100I$ using 166 energy groups and 155 spatial intervals. In addition, two AWMC calculations were made, one using 175 energy groups and 101 spatial intervals and another using 218 energy groups and 145 spatial intervals. The results of all four calculations are shown in Fig. 6 in the form of the total transmitted electron current per MeV per incident electron. The 218-group AWMC calculation represents a set of converged results and gives higher values and a more sharply peaked distribution than does the 176-group AWMC calculation. However, in order to achieve the converged results, the 218-group AWMC calculation requires a larger number of spatial intervals and a much longer run time than the 176-group AWMC run. The two AWCS calculations give fairly similar results, although the $I' = 100I$ calculation requires a larger number of spatial intervals and a longer run time than does the $I' = 10I$ run. It should also be noted that the $I' = 100I$ calculation gives a very strongly

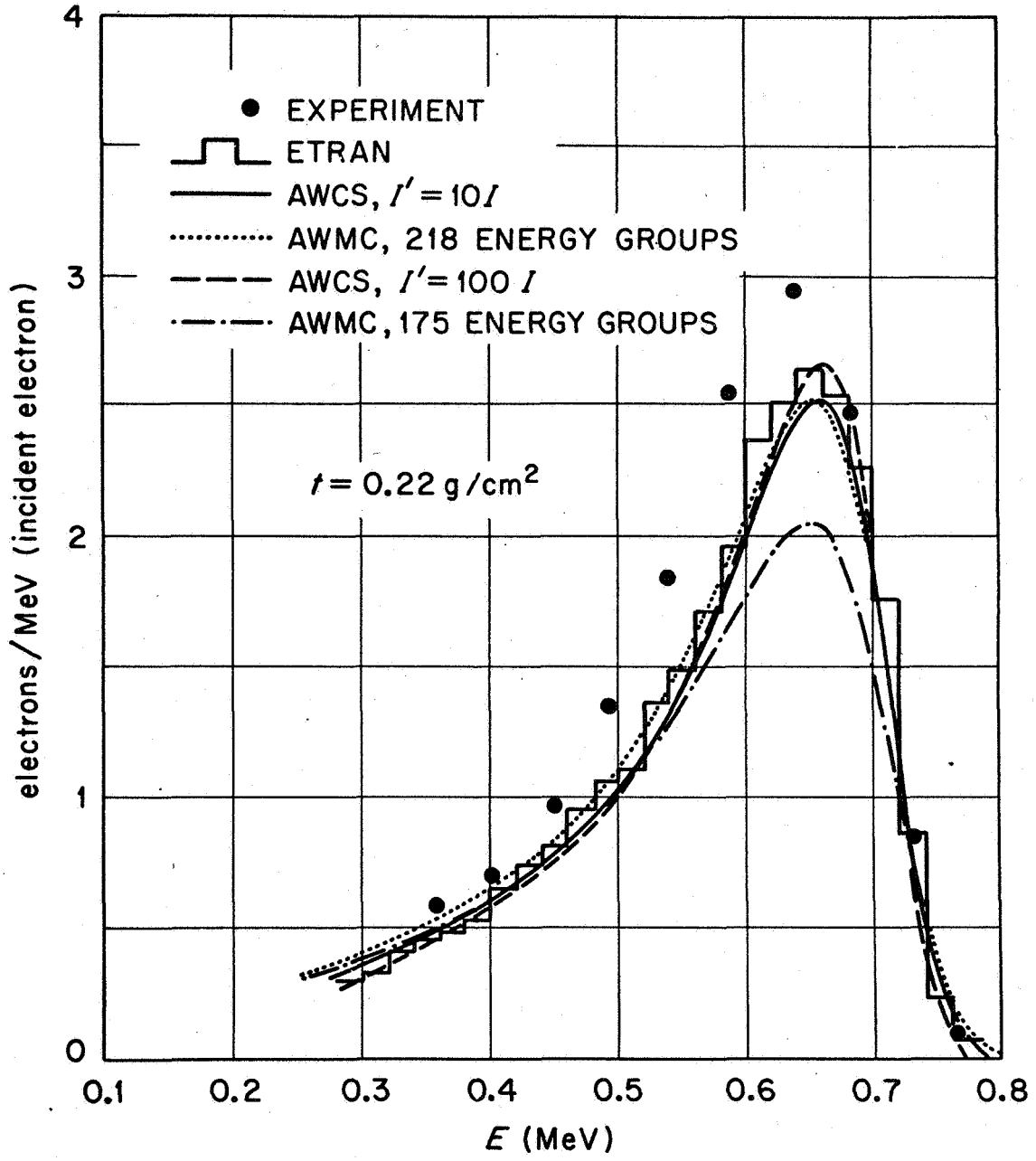

Fig. 6. Transmitted electron current per unit energy per incident electron for 1-MeV electrons normally incident on 0.22-g/cm^2-thick aluminum slabs.

forward-peaked angular distribution for a thin case (such as 0.10 g/cm^2), since the soft collisions are straightahead and the number of soft collisions increases as I' increases. In general, the AWCS method requires fewer energy groups, fewer spatial intervals, less time to produce the cross section coefficients, and a shorter time for calculational than the AWMC method requires in order to obtain converged results. Details on the calculations shown in Fig. 6 are given in the following table. The running times shown are for the IBM 360/91 computer. The cross-section production time represents the time required to produce the cross-section coefficients used for the particular calculation. Other calculations (especially for other target thicknesses) were frequently made with the same set of coefficients. The calculational time is the time required for ANISN to obtain a solution for the problem using the previously determined cross-section coefficients.

Table I. Requirements for the Discrete Ordinates Calculation Shown in Fig. 6

Discrete Ordinates Calculational Method	Number of Energy Groups	Number of Spatial Intervals	Time for ANISN Calculation (min.)	Time for Cross-Section Production (min.)
AWCS* (ANISN with continuous slowing-down $I' = 10I = 1.63 \times 10^{-3}$ MeV	160	100	11.5	18
AWCS $I' = 100I = 1.63 \times 10^{-2}$ MeV	166	155	35	15
AWMC* (ANISN with Møller cross-section)	218	145	44	24
AWMC	175	101	14.5	16

*This calculation also appears in Fig. 5.

The calculated and measured transmitted electron current per unit energy per unit solid angle is presented in Fig. 7 for transmission angles of 7.5°, 47.5° and 77.5° through a 0.10-g/cm^2-thick aluminum slab. Both the AWCS and AWMC calculations give good agreement with the experimental results at 7.5°, although the AWCS values are slightly high, probably due to the tendency of the AWCS calculation to produce a forward-peaked angular distribution for thin cases. Both discrete ordinates methods are in reasonable agreement with experiment at 47.5° and in poor agreement at 77.5°. It should be noted that the Monte Carlo results at 77.5° show evidences of difficulty with statistical accuracy.

The transmitted electron current for 1-MeV electrons through a 0.22-g/cm^2-thick aluminum slab at angles of 7.5°, 47.5°, and 77.5° is shown in Fig. 8. Both discrete ordinates calculational methods show good agreement with the measured results at 7.5°, except at the peak of the experimental distribution. Agreement with experiment is fair at 47.5° and poor at 77.5°, with the discrete ordinates results again being low. The angular transmission for the two discrete ordinates calculations were a little more consistent for the 0.22-g/cm^2 case than for the 0.10-g/cm^2 case. Presumably this occurs because the increase in target thickness allows sufficient elastic angular scattering so that the differences in the way in which the inelastic scattering is handled are not extremely significant.

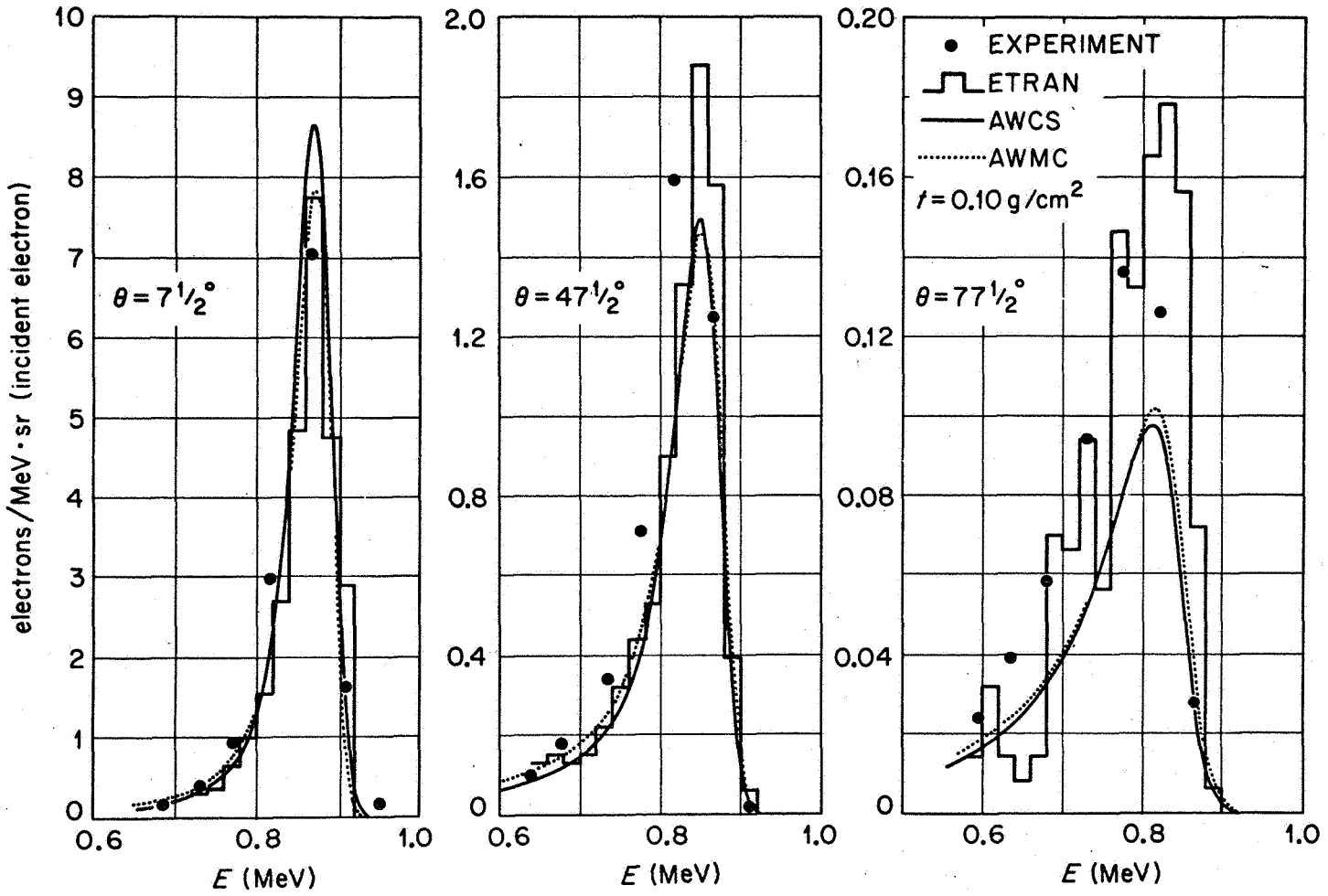

Fig. 7. Energy distributions of the transmitted electron current at 7.5°, 47.5°, and 77.5° for 1-MeV electrons normally incident on a 0.10-g/cm^2-thick aluminum slab.

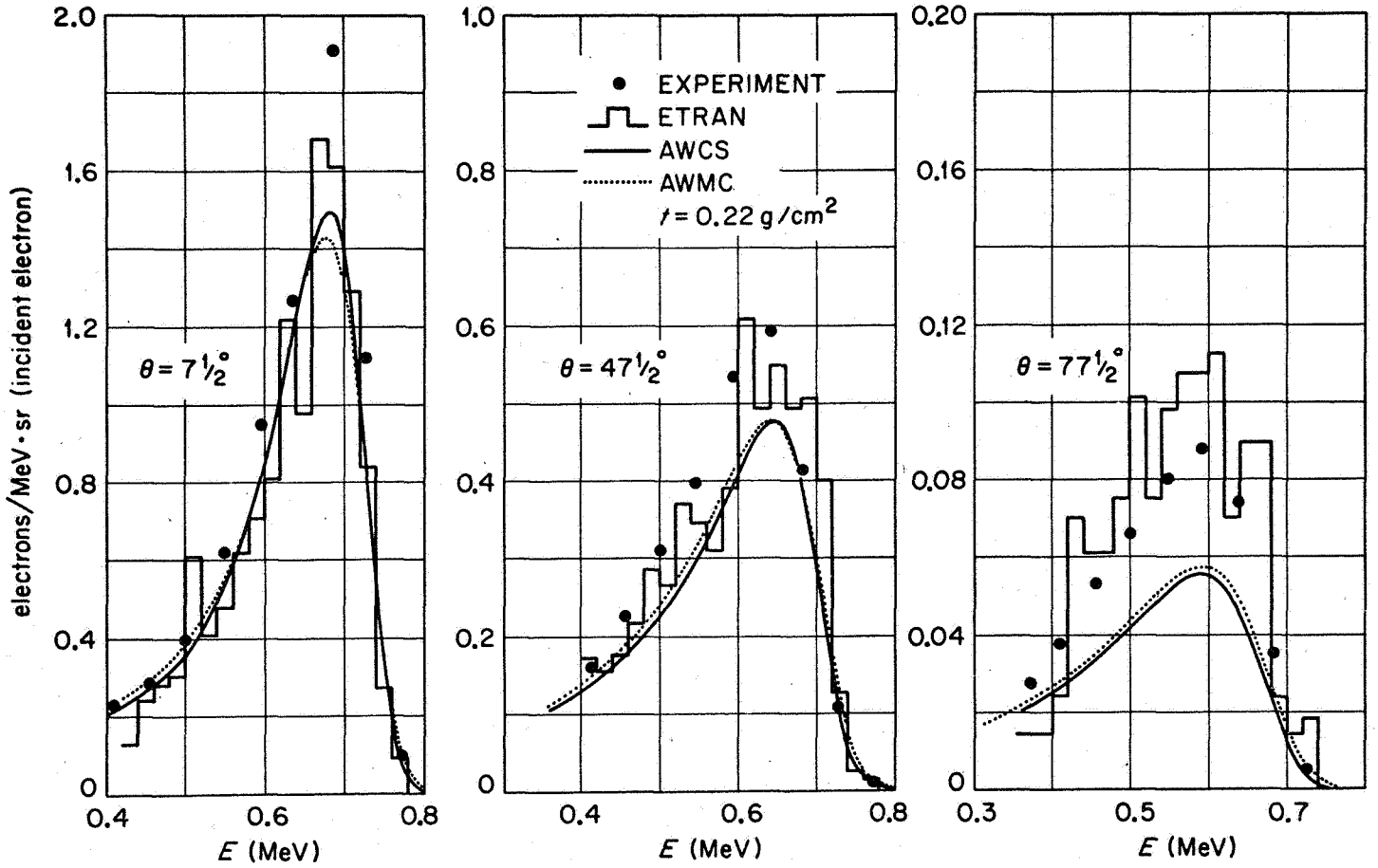

Fig. 8. Energy distributions of the transmitted electron current at 7.5°, 47.5°, and 77.5° for 1-MeV electrons normally incident on a 0.22-g/cm^2-thick aluminum slab.

The angular distributions of the transmitted electrons per unit solid angle resulting from 1-MeV electrons normally incident on 0.10-g/cm^2, 0.22-g/cm^2, and 0.32-g/cm^2-thick aluminum slabs are presented in Fig. 9. The AWCS calculation does show a slightly forward-peaked distribution in the 0.10-g/cm^2 case, but is in good agreement with the experimental values. The AWMC results show reasonable agreement for the 0.10-g/cm^2 slab. The discrete ordinates calculations are very similar for the 0.22-g/cm^2 case, and are in reasonable agreement with experiment. In the 0.32-g/cm^2 case, the AWCS values are in good agreement with experiment, while the agreement for AWMC is only fair. The higher results for AWCS are similar to those shown in Fig. 5 for the total transmitted electron current for 0.32 g/cm^2.

2. <u>1-MeV Electrons Incident on Gold</u>

The total transmitted electron current per unit energy resulting from 1-MeV electrons normally incident on a 0.15-g/cm^2-thick gold slab, representing 0.2 range, is shown in Fig. 10a. The experimental points and Monte Carlo histogram are similar to those used earlier for the aluminum cases, and the solid curve represents the results of a discrete ordinates AWCS calculation with $I' = I(7.97 \times 10^{-4}$ MeV). This value was used because it is close to the value used for the 1-MeV aluminum runs ($I' = 1.63 \times 10^{-3}$ MeV). The discrete ordinates results are much lower than the experimentally measured values and significantly lower than the Monte Carlo calculation. Additional work is necessary to determine if the poor agreement noted here is due to the cross

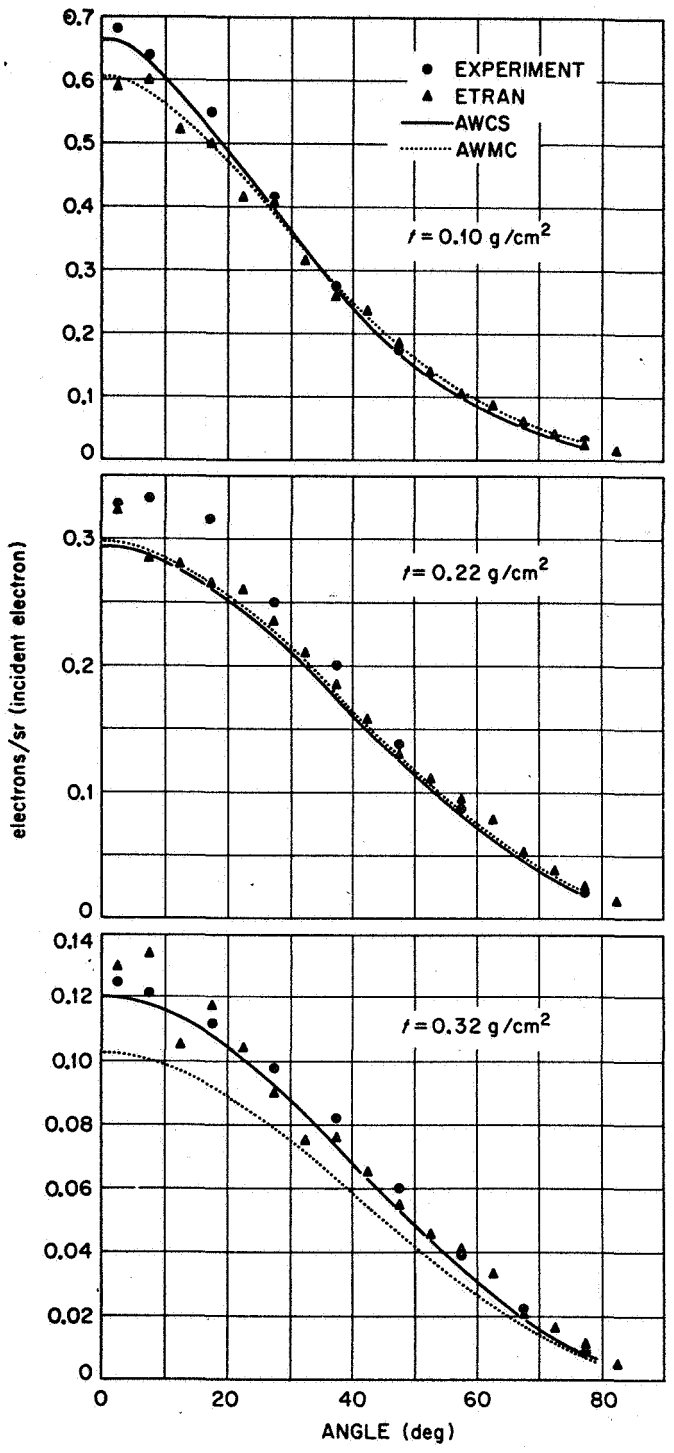

Fig. 9. Angular distributions of the transmitted electron current for 1-MeV electrons normally incident on 0.10-g/cm^2-, 0.22-g/cm^2-, and 0.32-g/cm^2-thick aluminum slabs.

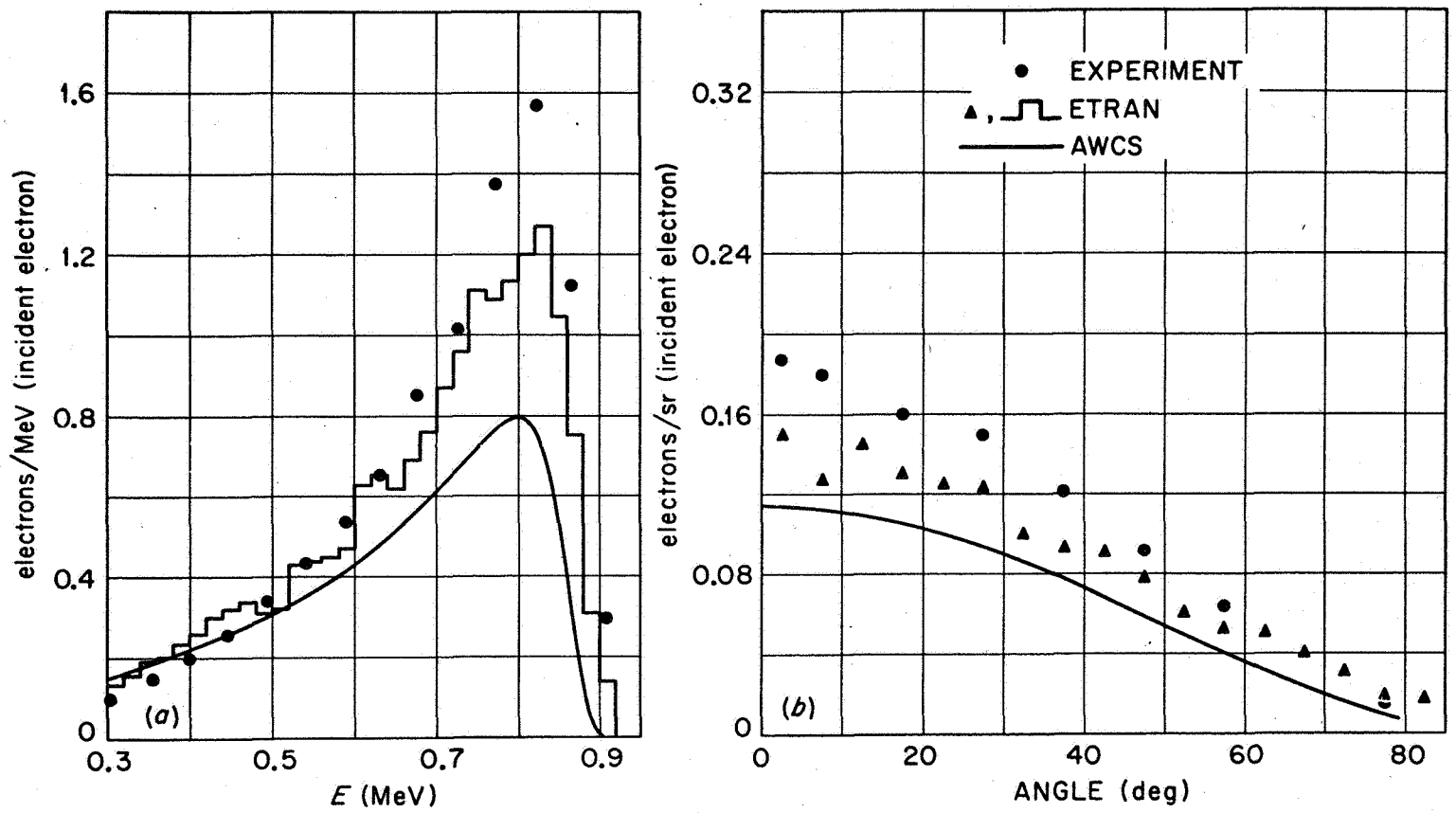

Fig. 10.(a) Transmitted electron current per unit energy per incident electron for 1-MeV electrons normally incident on a 0.15-g/cm^2-thick gold slab. (b) Angular distribution of the transmitted electron current for 1-MeV electrons normally incident on a 0.15-g/cm^2-thick gold slab.

sections or to the method of the calculation itself. At least part of the difficulty must be in the cross sections, since the hard inelastic atomic cross section was determined by multiplying the Møller cross section by Z. This is obviously incorrect since the K shell electrons in gold are far too tightly bound to be considered free, but no tested correction factor was available. The angular distribution of the transmitted electron current per unit angle for this case is given in Fig. 10b. It shows the distribution calculated by discrete ordinates to be much smaller at low angles than the experimental distribution, as is expected from Fig. 10a, but that it increases in relation to the experimental points at larger angles. The same general behavior is shown by the Monte Carlo calculation of the distribution, which is lower than the experimental measurement at low angles but actually higher at large angles.

3. 2.5-MeV Electrons Incident on Aluminum

The points plotted in Fig. 11 show the total transmitted electron current per unit energy per incident electron resulting from 2.5-MeV electrons normally incident on 0.31-g/cm^2(0.2 range) and 0.62-g/cm^2-(0.4 range) thick aluminum slabs. The experimental points, Monte Carlo histograms, AWCS and AWMC representations are similar to those used for the 1-MeV case. Reasonable agreement is shown between the discrete ordinates results and the experimental measurements in both cases.

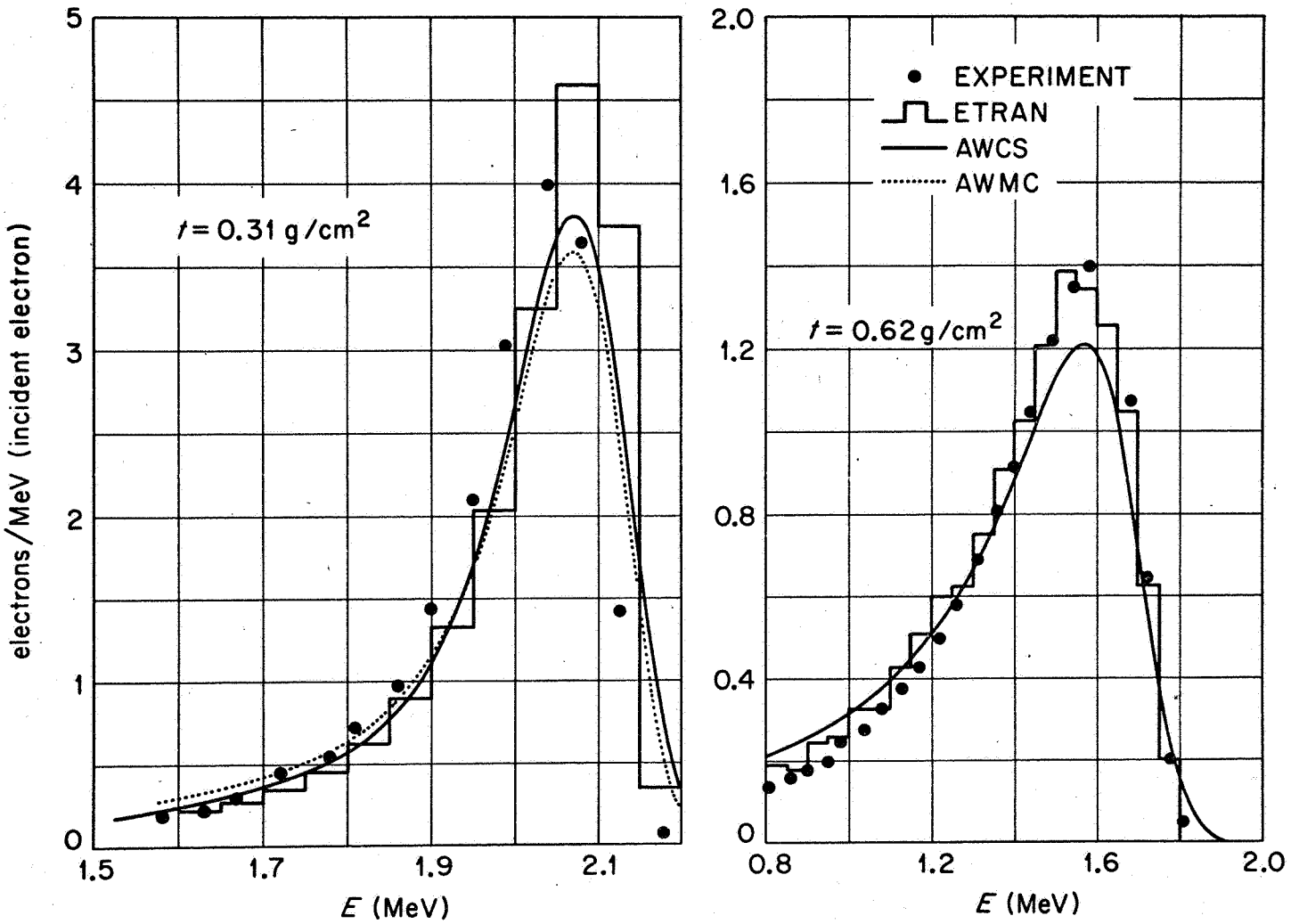

Fig. 11. Transmitted electron current per unit energy per incident electron for 2.5-MeV electrons normally incident on 0.31-g/cm^2-thick and 0.62-g/cm^2-thick aluminum slabs.

However, the discrete ordinates calculations here are somewhat lower than the Monte Carlo values, especially at the peak of the distribution, while agreement between discrete ordinates and Monte Carlo calculations is good for the 1-MeV cases.

The transmitted electron current at 20°, 45°, and 60° resulting from 2.5-MeV electrons normally incident on a 0.31-g/cm^2-thick aluminum slab is shown in Fig. 12. The calculated values at 20° are in fair agreement with the experimental points, but at 45° the agreement is poor at the peak of the distribution, with the calculated results higher than the experimental results. At 60°, the discrete ordinates calculations are considerably higher than the experimental measurements over most of the distribution. This seems to contradict the large-angle calculations for the 0.2 range 1-MeV case, where the calculated values were low compared to experiment (see Fig. 7). The reason for this phenomenon is not apparent.

The transmitted electron current at 10° and 20° resulting from 2.5-MeV electrons normally incident on a 0.62-g/cm^2-thick aluminum slab is given in Fig. 13. Agreement between the AWCS calculation and experimental measurements is poor at the peak of the distribution for both cases but is quite reasonable elsewhere. The low calculational results shown here are somewhat consistent with the slightly low peak values shown in Fig. 11 for the total transmitted current through the 0.62-g/cm^2 slab.

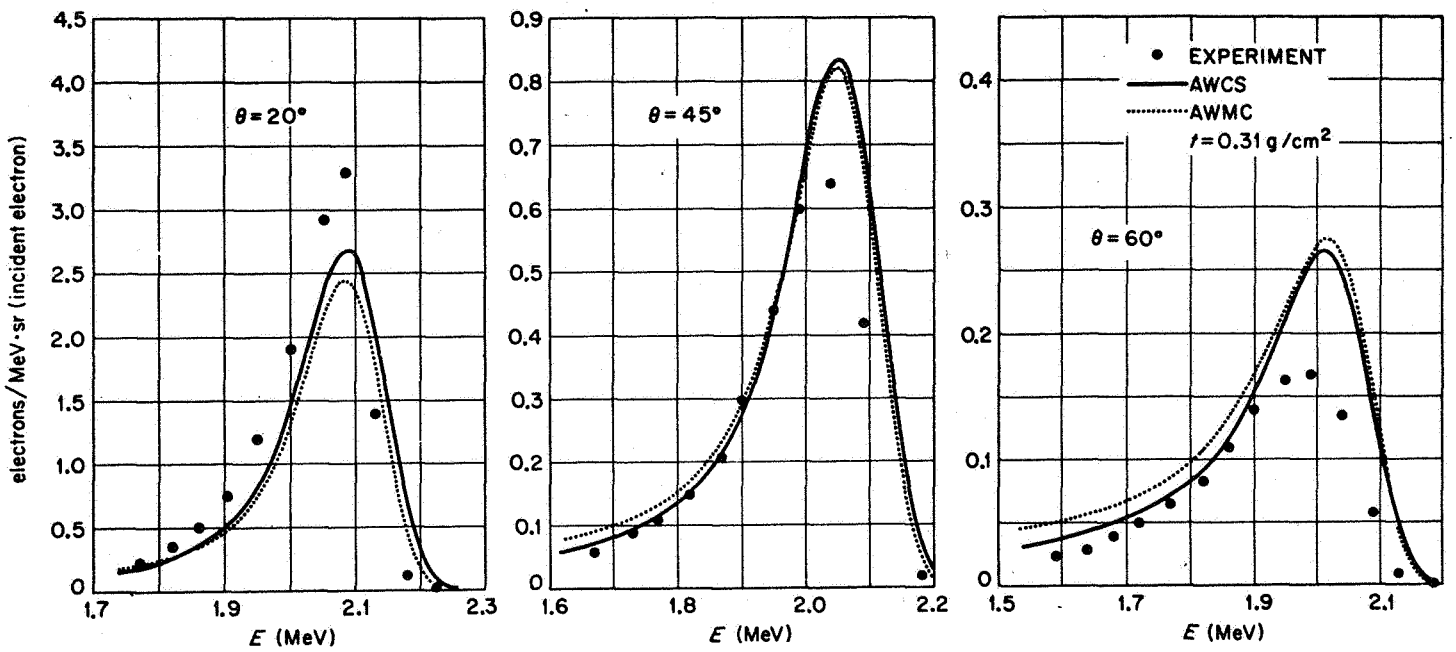

Fig. 12. Energy distributions of the transmitted electron current at 20°, 45°, and 60° for 2.5-MeV electrons normally incident on a 0.31-g/cm^2-thick aluminum slab.

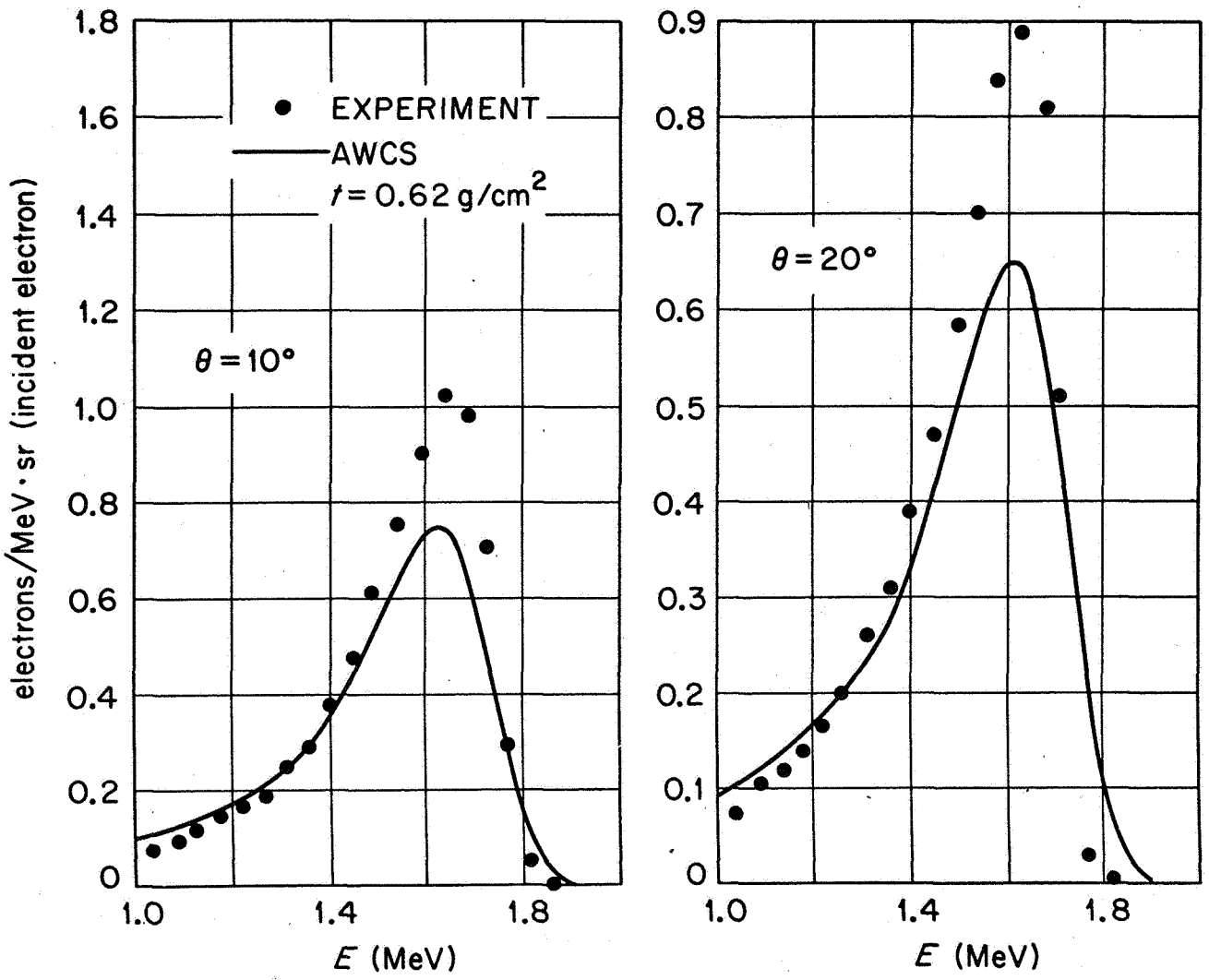

Fig. 13. Energy distributions of the transmitted electron current at 10° and 20° for 2.5 MeV electrons normally incident on a 0.62-g/cm^2-thick aluminum slab.

The angular distributions of the transmitted electron current per unit solid angle for 2.5-MeV electrons normally incident on 0.31-g/cm^2 and 0.62-g/cm^2-thick aluminum slabs are presented in Fig. 14. The values calculated by the discrete ordinates methods for the 0.31-g/cm^2 case are higher than the experimental measurements through much of the distribution, as was shown in Fig. 12. The Monte Carlo calculations also follow this general tendency. The AWCS results for the 0.62-g/cm^2 case show more reasonable agreement with the experimental values, although the calculation is slightly low at the forward angles.

B. Experiments of Lonergan et.al.

The experimental data presented here are taken from the work of Lonergan, Jupiter, and Merkel.[27] The Monte Carlo calculations were made by Edmondson, Derrickson and Peasley* using ETRAN-15.[3] Results are given for 4-MeV and 8-MeV electrons incident on aluminum targets.

1. 4-MeV Electrons Incident on Aluminum

The electron current per unit energy per unit solid angle transmitted at 30° from 4-MeV electrons normally incident on a 1.275-g/cm^2-thick aluminum slab (0.5 range) is given in Fig. 15a. The experimental points and Monte Carlo histogram are plotted in the usual manner, and the solid curve represents an AWCS discrete ordinates calculation with $I' = 10I(1.63 \times 10^{-3}$ MeV). Agreement between the discrete ordinates results and the experimental measurements is fair,

*As mentioned in Ref. 27.

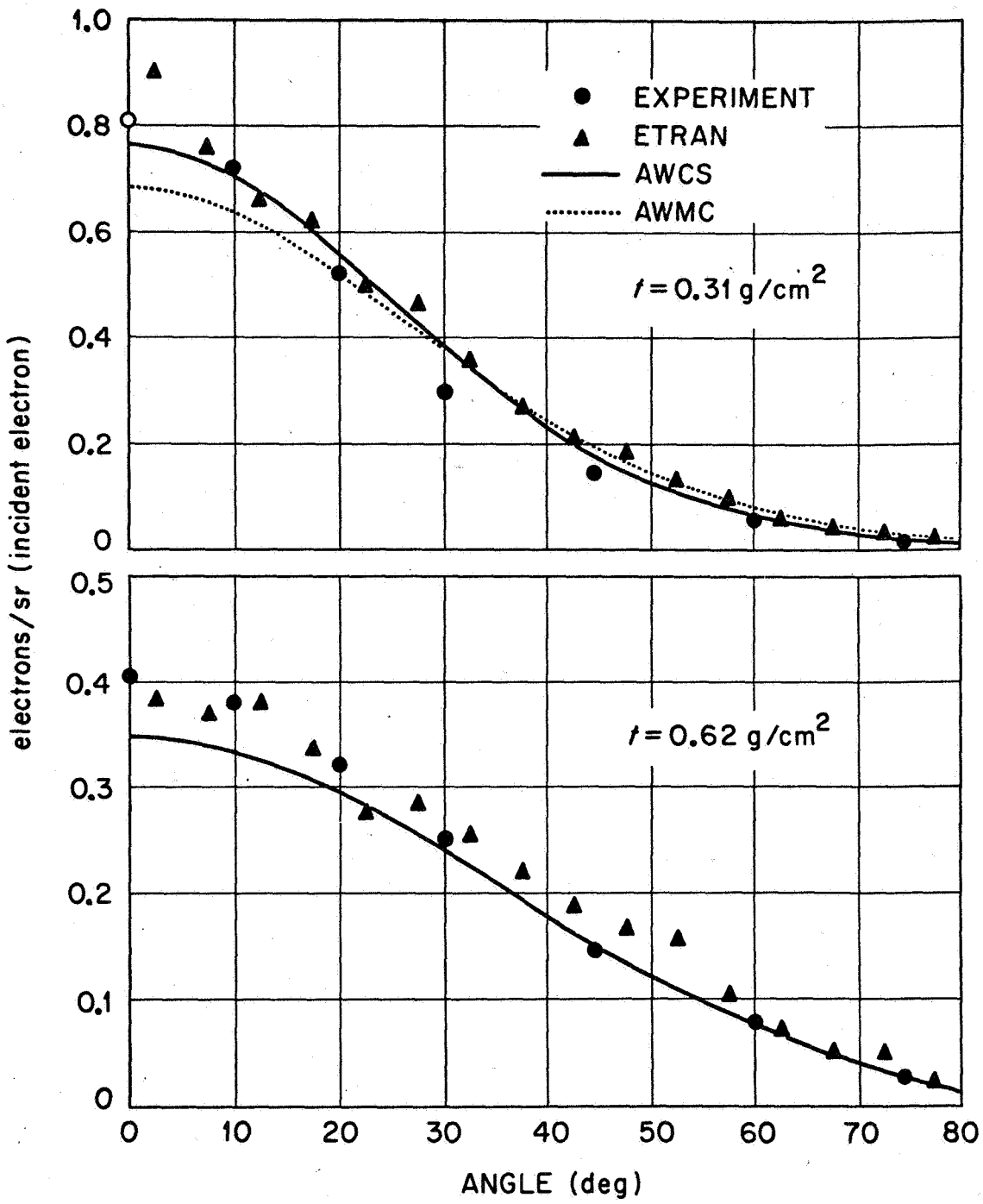

Fig. 14. Angular distributions of the transmitted electron current for 2.5-MeV electrons normally incident on 0.31-g/cm^2-thick and 0.62-g/cm^2-thick aluminum slabs.

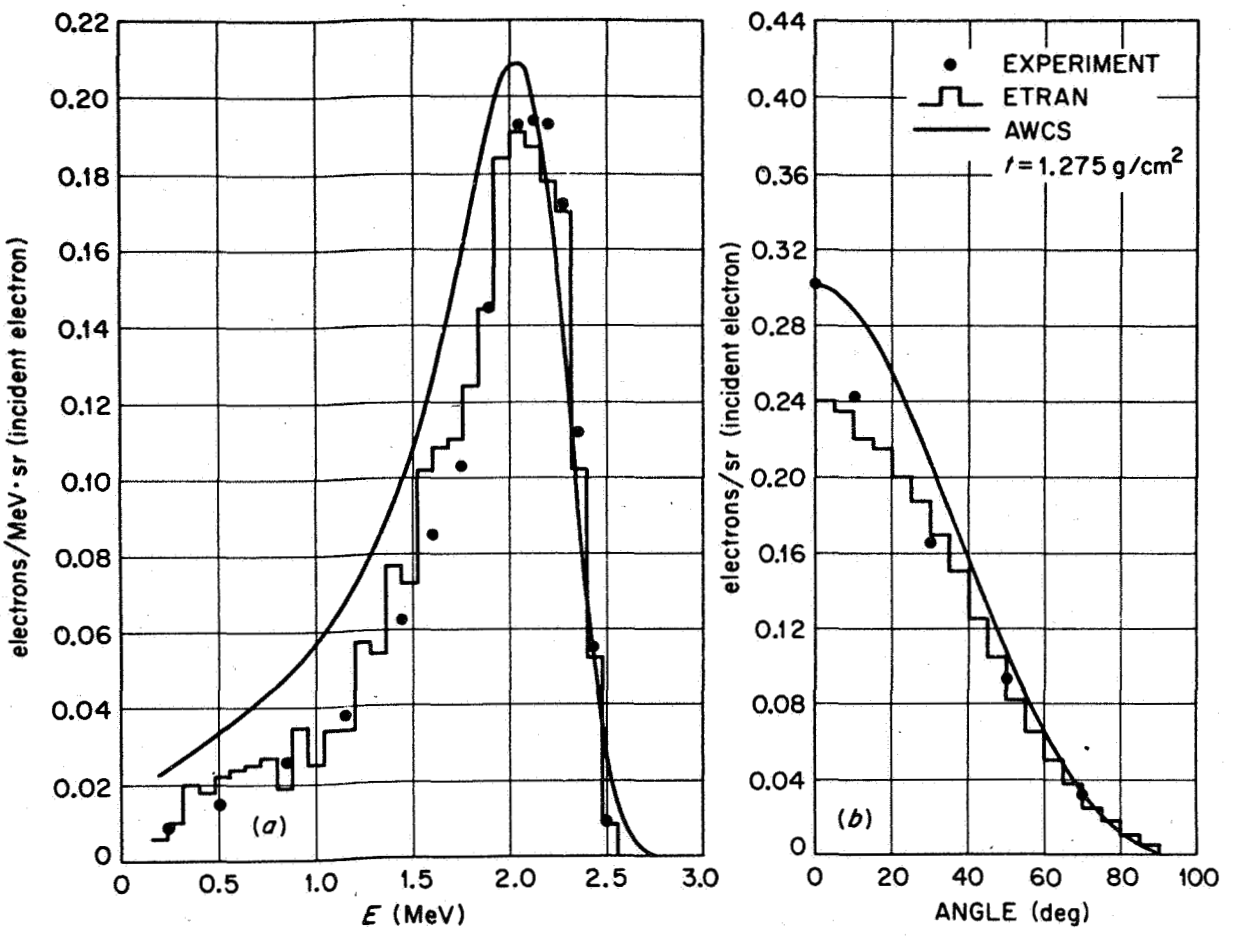

Fig. 15.(a) Energy distribution of the transmitted electron current at 30° for 4-MeV electrons normally incident on a 1.275-g/cm^2-thick aluminum slab. (b) Angular distributions of the transmitted electron current for 4-MeV electrons normally incident on a 1.275-g/cm^2-thick aluminum slab.

while the agreement between the Monte Carlo values and experiment is much better. However, in the summary of Ref. 27 it states "The number of 4.0 MeV electrons transmitted through 1.275-g/cm^2-thick slabs of Al was 25% higher in the calculation. When the calculated energy spectra and angular distribution were renormalized to the experimental transmission they agreed with the measured data." Since the AWCS calculation is considerably higher than the experimental results and the Monte Carlo values at the peak and at lower energies in the distribution, it seems quite possible that the agreement between the AWCS results and the Monte Carlo calculation before renormalization might be better than that shown in Fig. 15a.

The angular distribution of the transmitted electron current per unit solid angle from 4-MeV electrons normally incident on a 1.275-g/cm^2-thick aluminum slab is shown in Fig. 15b. The AWCS values are considerably higher over most of the distribution than the Monte Carlo results and those from the experimental measurements, as would be expected from Fig. 15b. It is interesting to note, however, that the discrete ordinates value at 0° is very close to the experimental point, while the Monte Carlo histogram is much lower.

2. <u>8-MeV Electrons Incident on Aluminum</u>

The electron current per unit energy per unit solid angle transmitted at 20° from 8-MeV electrons normally incident on a 0.953-g/cm^2-thick aluminum slab (0.2 range) is given in Fig. 16a. The experimental points, Monte Carlo histogram, and AWCS using I' = 10I are shown as in previous figures. The discrete ordinates calculation shows excellent

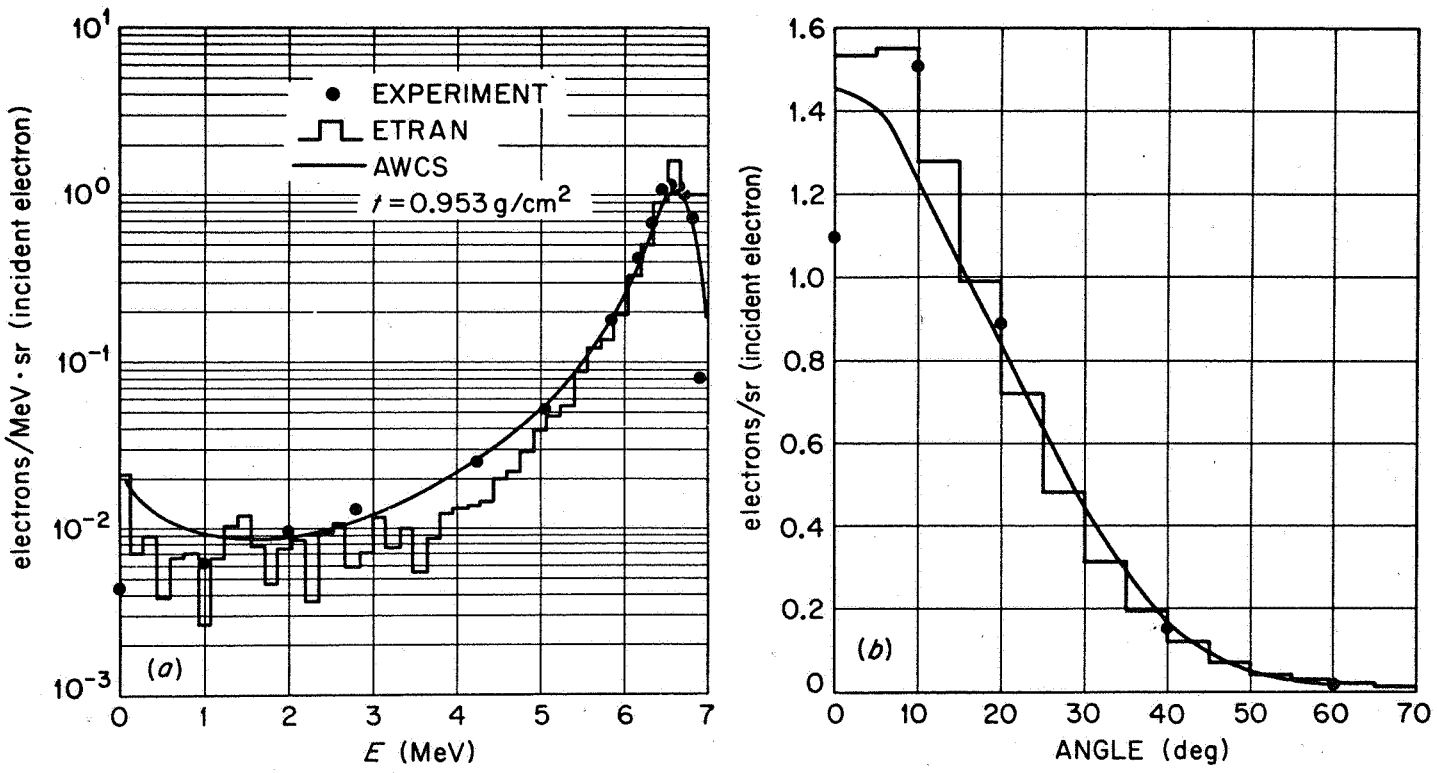

Fig. 16.(a) Energy distribution of the transmitted electron current at 20° for 8-MeV electrons normally incident on a 0.953-g/cm^2-thick aluminum slab. (b) Angular distribution of the transmitted electron current for 8-MeV electrons normally incident on a 0.953-g/cm^2-thick aluminum slab.

agreement with the experimental measurements over most of the energy range. However, the calculated curve actually increases in value below 2 MeV, while the experimentally measured points continue to decrease in magnitude. It should be noted that the Monte Carlo calculation, although exhibiting some statistical fluctuation, also appears to increase in the lower energy range.

The angular distribution of the transmitted electron current per unit solid angle for 8-MeV electrons normally incident on a 0.953-g/cm^2-thick aluminum slab is presented in Fig. 16b. The distribution from the discrete ordinates calculation is in excellent agreement with the experimental points at the higher angles, but is does not exhibit a low-angle peak as the experimental distribution does. The low-angle peak in Fig. 16b. is in sharp contrast to the high experimental value at 0° shown in Fig. 15b.

VII. COMPARISON WITH A THEORETICAL CALCULATION FOR AN INCIDENT ELECTRON SPECTRUM

A. Transmitted Electron Spectra

Because of the lack of experimental data, it was not possible to present a comparison between calculated and experimental results for the case of an electron energy spectrum incident on a slab. Using the Monte Carlo code ETRAN of Berger and Seltzer,[3] Scott[48] calculated the transmitted electron current per unit energy for the case of a specific electron energy spectrum normally incident on aluminum slabs, and this theoretical calculation has been compared with results obtained with ANISN. The incident electron energy distribution used in the calculations is a representation of the spectrum resulting from thermal-neutron capture in ^{235}U.[49] This spectrum extends to electron energies of the order of 10 MeV and is shown explicitly in Fig. 17 (taken from Ref. 48). The transmitted electron current was calculated by the continuous slowing-down version of ANISN from Eq. (16). Inelastic collisions with atomic electrons involving an energy transfer greater than I' were represented by the Møller cross section, Eq. (19). Those with an energy transfer less than I' were approximated by a continuous slowing-down term. The I' value used for this calculation was 100 I, or 0.0163 MeV. The ANISN calculation used 21 electron energy groups down to 0.15 MeV and 320 spatial intervals for 1.0-g/cm^2 thickness. The ETRAN results for an aluminum slab 0.5-g/cm^2 thick are shown in Fig. 18 as a histogram and the ANISN results are shown as plotted points. A similar comparison is given in Fig. 18 for an aluminum slab 1.0-g/cm^2 thick.

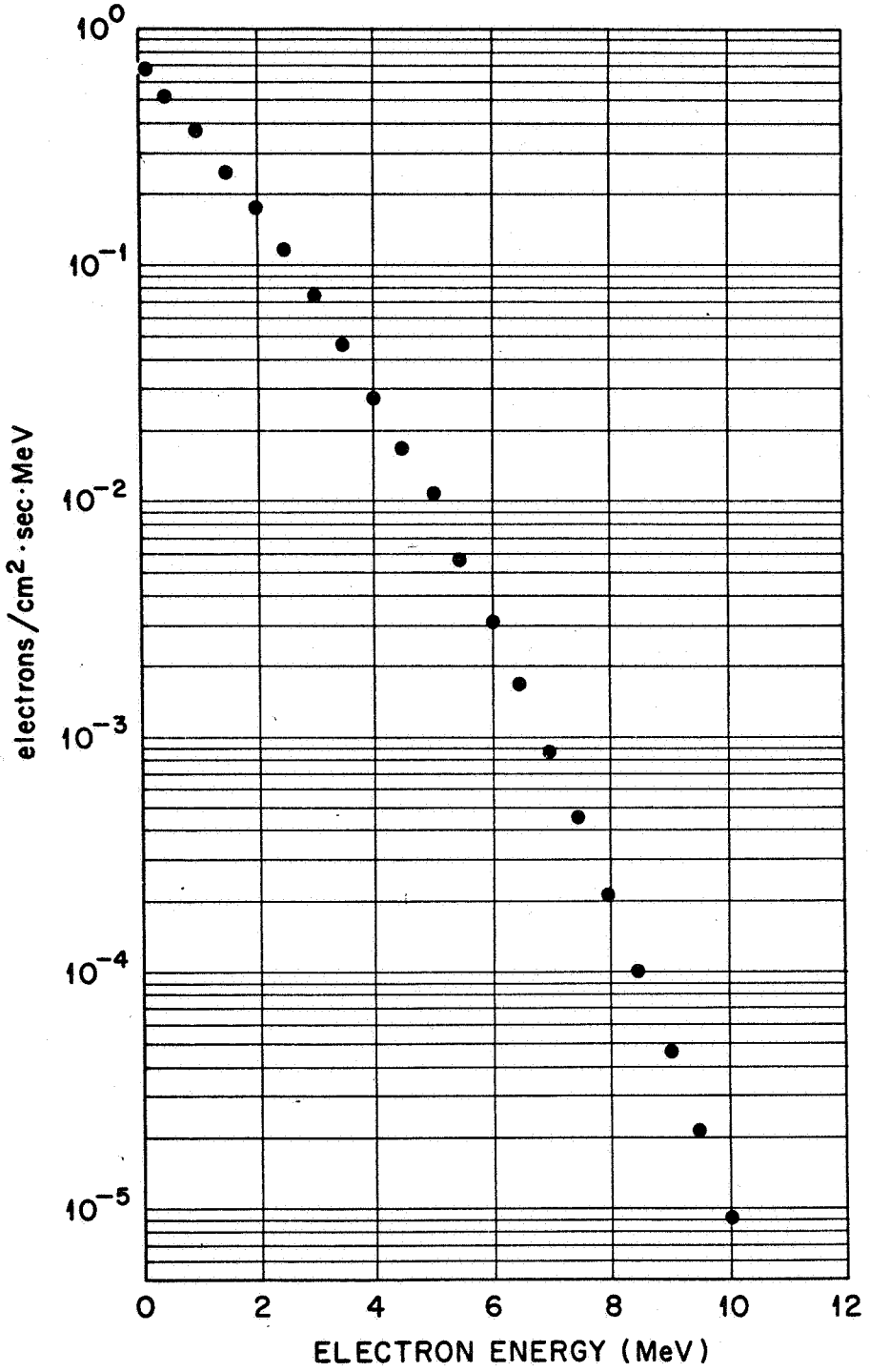

Fig. 17. Energy distribution of the incident electron current per unit energy per incident electron used by Scott[48] as a source.

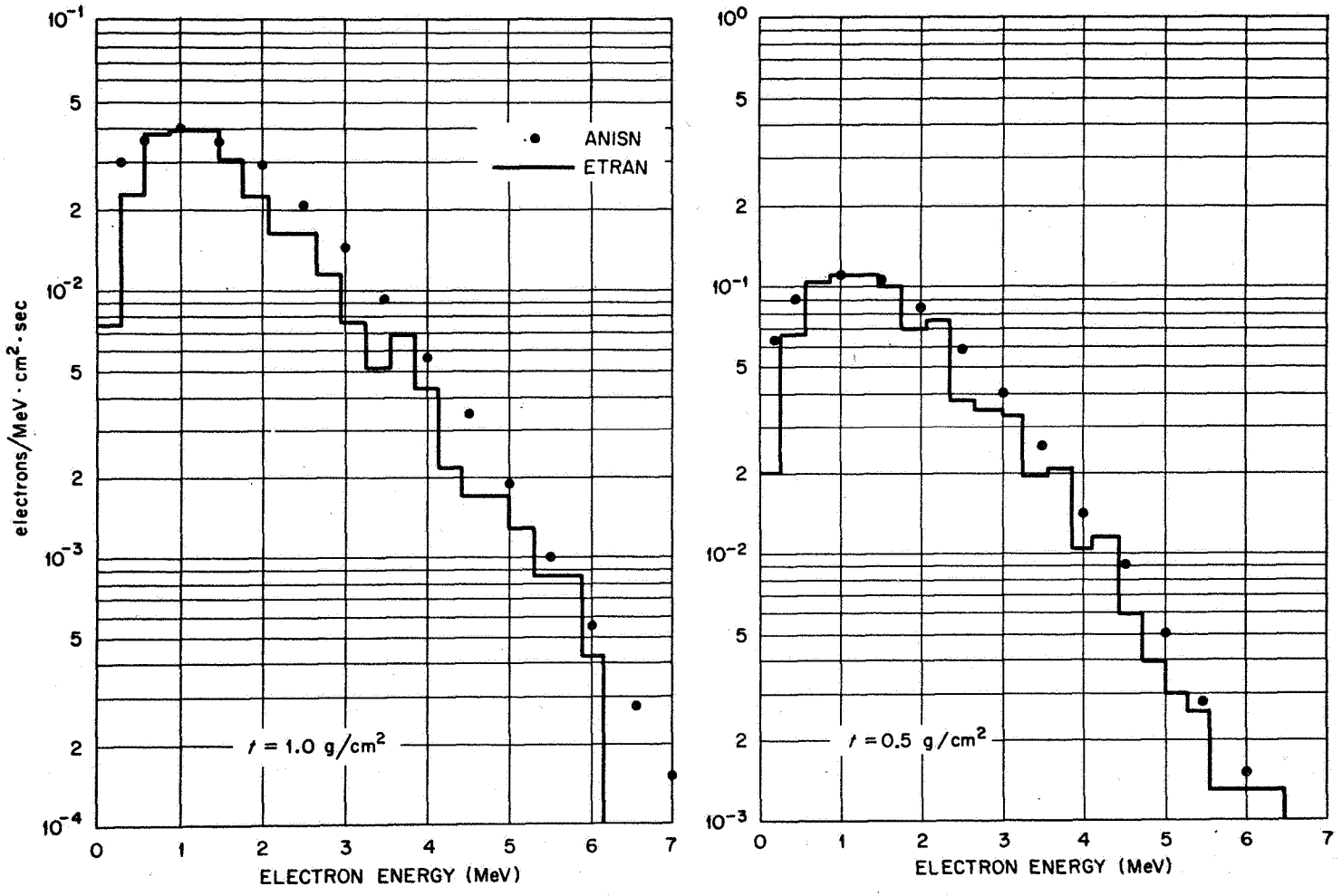

Fig. 18. Transmitted electron current per unit energy per incident electron for a specific energy spectrum (Fig. 17) normally incident on 0.50-g/cm^2-thick and 1.0-g/cm^2-thick aluminum slabs.

In both plots the ETRAN and ANISN results are in reasonable agreement, although the ANISN results are a little high in the 2- to 4-MeV range for the 1.0-g/cm^2 case.

B. Transmitted Photon Spectra

In addition to the electron transport calculation, the photon current produced by bremsstrahlung was computed and transported through the slab by solving Eq. (2) for photon transport coupled with Eq. (16) for electrons. As indicated in Section III, this coupling introduces photons produced by electron bremsstrahlung as a source for the photon transport equation, but electrons produced by photons are not introduced into the electron transport equation. The photon calculation used 60 energy groups down to 0.01 MeV and a total of 339 intervals for a 50-g/cm^2-thick aluminum slab. At thick depths the primary electrons are no longer present, and photons constitute the bulk of the dose at such depths. Electrons are present, produced by the photons, but the photons are dominant. The method of discrete ordinates is quite capable of calculating the resulting photon current, even for very thick target depths, as shown in Fig. 19. It would be very difficult to obtain reasonable statistical accuracy in a similar calculation by a Monte Carlo procedure.

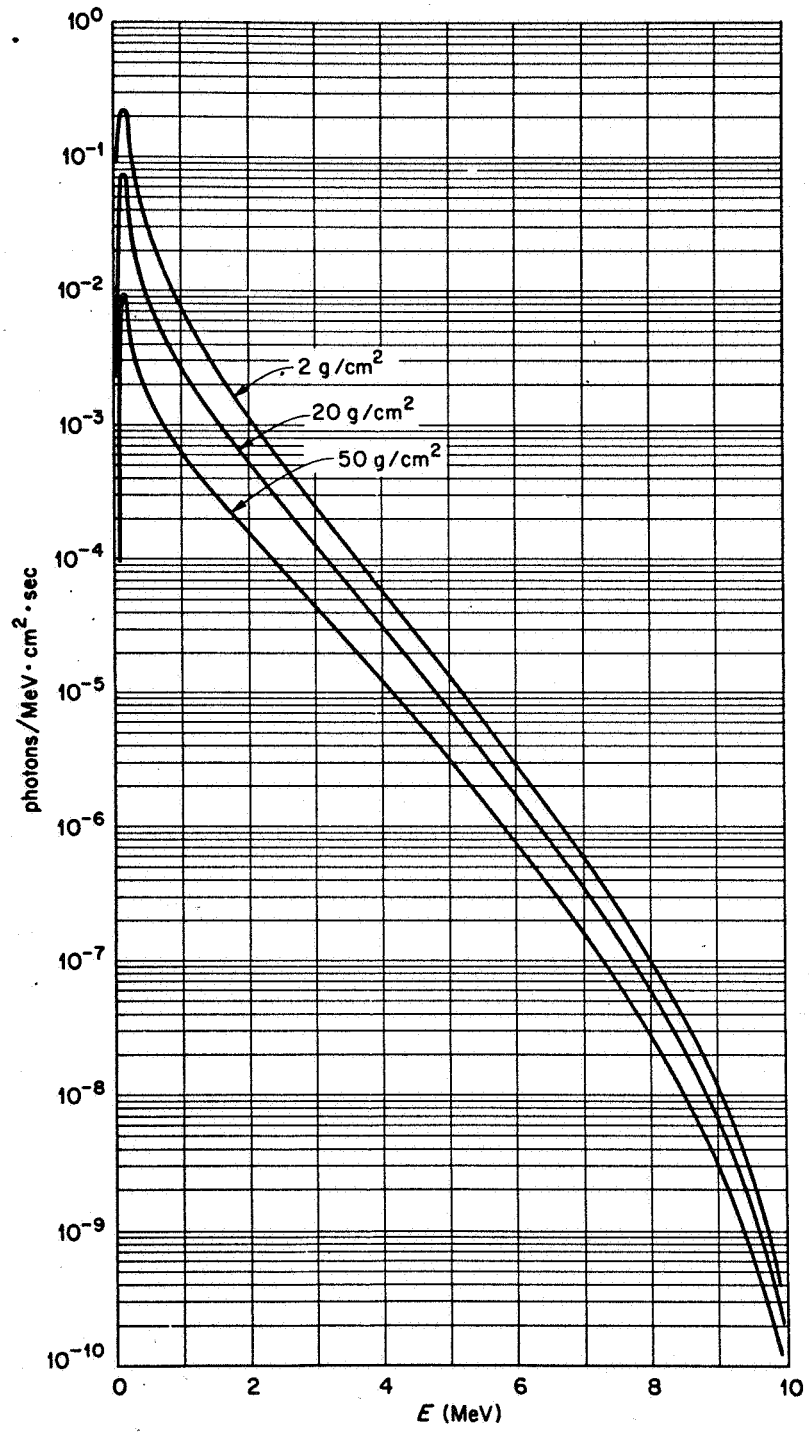

Fig. 19. Transmitted photon current per unit energy per incident electron for a specific energy spectrum of electrons (Fig. 17) normally incident on aluminum slabs of the thicknesses indicated.

VIII. CONCLUSIONS AND RECOMMENDATIONS

Discrete ordinates appears to be a very promising method for calculating the transport of electrons in aluminum, but additional investigation is required to determine the extent of its applicability. The results achieved for electron transport through gold are considerably poorer than the calculations for aluminum. It seems probable that the difference in the results achieved is due to the difference between heavy elements (Au) and light elements (Al). It is not known whether the difficulty experienced with gold is due to the method of calculation or to the cross sections employed, but it seems more likely that the problem lies in the cross sections.

Both ANISN with continuous slowing down used to treat low-energy transfer collisions (AWCS) and ANISN with the Møller cross section used to treat low-energy transfer collisions (AWMC) are capable of giving acceptable results for aluminum. At this stage of development, AWCS seems preferable because it requires fewer energy groups to produce converged results and requires a shorter running time than does AWMC.

Subsequent areas of investigation should include calculations for several nonaluminum targets in order to determine the range of applicability of the method of calculation and of the current cross sections. An attempt should then be made to develop the cross-section theories for heavy elements in order to get agreement with the experimental results. Calculations should also be made for comparison with experimental studies of electron bremsstrahlung.

Calculation of electron transport by discrete ordinates could be made more efficient by a more precise determination of the energy-group structure required to achieve converged results for both monoenergetic and energy-spectrum sources. The calculational procedure in ANISN could be made more efficient for electrons by limiting the application of the convergence criteria for a particular energy group to those spatial intervals where the calculated electron current for that group is significant. In addition, a weighting function might be used to reduce the number of energy groups required for a calculation. Weighting functions are often used in the process of treating cross sections to obtain a multigroup form[24] and normally involve the representation of several groups from a normal energy group structure by a single energy group with an averaged cross section.

The averaging procedure includes weighting the cross sections in the original group structure by some measure of their relative importance. However, recent work on neutron transport in iron[50] shows that although significant improvement can be obtained by the selection of a good weighting function, some problems require a specific group structure in order to obtain precise answers.

APPENDICES

APPENDIX A

DERIVATION OF THE CONTINUOUS SLOWING-DOWN TRANSPORT EQUATION

The derivation given here follows the method used by Rossi.[31] The Boltzmann transport equation for electrons is given by Eq. (11) as

$$\vec{\Omega}\cdot\nabla\phi(\vec{R},E,\vec{\Omega}) = P(\vec{R},E,\vec{\Omega}) + n \int_{E}^{E_o} dE' \int d\Omega' \frac{d^2\sigma^*_{e\to e}(E',E,\vec{\Omega}'\cdot\vec{\Omega})}{dEd\Omega} \phi(\vec{R},E',\vec{\Omega}')$$

$$+ n \int_{E+I'}^{E_o} dE' \int d\Omega' \frac{d^2\sigma_{inel}(E',E,\vec{\Omega}'\cdot\vec{\Omega})}{dEd\Omega} \phi(\vec{R},E',\vec{\Omega}')$$

$$- n\, \sigma_1^T(E)\, \phi(\vec{R},E,\vec{\Omega})$$

$$+ n \int_{E}^{E+I'} dE' \int d\Omega' \frac{d^2\sigma_{inel}(E',E,\vec{\Omega}'\cdot\vec{\Omega})}{dEd\Omega} \phi(\vec{R},E',\vec{\Omega}')$$

$$- n\, \sigma_2^T(E)\, \phi(\vec{R},E,\vec{\Omega}) - n\, \sigma^*_{e\to e}(E)\, \phi(\vec{R},E,\vec{\Omega}) \quad , \tag{34}$$

where

$$\sigma^*_{e\to e} = \sigma_{el} + \sigma_{br} \, ,$$

$$\sigma_1^T(E) = \int_{\frac{E}{2}}^{E-I'} dE' \int d\Omega \frac{d^2\sigma_{inel}(E,E',\vec{\Omega}'\cdot\vec{\Omega})}{dE'd\Omega} \, ,$$

$$\sigma_2^T(E) = \int_{E-I'}^{E} dE' \int d\Omega \frac{d^2\sigma_{inel}(E,E',\vec{\Omega}'\cdot\vec{\Omega})}{dE'd\Omega} \, .$$

The inelastic scattering is now separated into terms describing large and small energy transfer collisions. Define

$$T = n \int_{E}^{E+I'} dE' \int d\Omega' \frac{d^2\sigma_{inel}(E',E,\vec{\Omega}'.\vec{\Omega})}{dEd\Omega} \phi(\vec{R},E',\vec{\Omega}') - n\sigma_2^T(E)\ \phi(\vec{R},E,\vec{\Omega}) \ , \tag{35}$$

where T describes small energy transfer collisions. Add and subtract

$$n \int_{E}^{E+I'} dE' \frac{d\sigma_{inel}(E',E)}{dE} \phi(\vec{R},E',\vec{\Omega}) \ ,$$

where

$$\frac{d\sigma_{inel}(E',E)}{dE} = \int d\Omega \frac{d^2\sigma_{inel}(E',E,\vec{\Omega}'.\vec{\Omega})}{dEd\Omega} \ ,$$

$$= \int d\Omega' \frac{d^2\sigma_{inel}(E',E,\vec{\Omega}'.\vec{\Omega})}{dEd\Omega} \ .$$

Then

$$T = n \int_{E}^{E+I'} dE' \int d\Omega' \frac{d^2\sigma_{inel}(E',E,\vec{\Omega}'.\vec{\Omega})}{dEd\Omega} \phi(\vec{R},E',\vec{\Omega}')$$

$$- n\ \sigma_2^T(E)\ \phi(\vec{R},E,\vec{\Omega})$$

$$+ n \int_{E}^{E+I'} dE' \frac{d\sigma_{inel}(E',E)}{dE} \phi(\vec{R},E',\vec{\Omega})$$

$$- n \int_{E}^{E+I'} dE' \frac{d\sigma_{inel}(E',E)}{dE} \phi(\vec{R},E',\vec{\Omega}) \ . \tag{36}$$

Now assume

$$\frac{d^2\sigma_{inel}(E',E,\vec{\Omega}'\cdot\vec{\Omega})}{dEd\Omega} = \frac{d^2\sigma_{inel}(E',E)}{dE} \times \frac{\delta(1-\vec{\Omega}'\cdot\vec{\Omega})}{2\pi} ,$$

that is, the soft collisions involve only an energy degradation and not an angular change. The first and last terms in Eq. (36) then cancel, and

$$T = n \int_E^{E+I'} dE' \frac{d\sigma_{inel}(E',E)}{dE} \phi(\vec{R},E',\vec{\Omega})$$

$$- n\, \sigma_2^T(E)\, \phi(\vec{R},E,\vec{\Omega}) ,$$

$$T = n \int_E^{E+I'} dE' \frac{d\sigma_{inel}(E',E)}{dE} \phi(\vec{R},E',\vec{\Omega})$$

$$- n \int_{E-I'}^{E} dE' \frac{d\sigma_{inel}(E,E')}{dE'} \phi(\vec{R},E,\vec{\Omega}) . \qquad (37)$$

Define

$$f(E',E) = \frac{d\sigma_{inel}(E',E)}{dE} \phi(\vec{R},E',\vec{\Omega})$$

$$\varkappa = E' - E , \quad d\varkappa = dE' , \quad \text{first term;}$$

$$\hat{\varkappa} = E - E' , \quad d\hat{\varkappa} = -dE' , \quad \text{second term.}$$

Then

$$T = n \int_0^{I'} d\varkappa\, f(E+\varkappa,E)$$

$$- n \int_0^{I'} d\hat{\varkappa}\, f(E,E-\hat{\varkappa}) . \qquad (38)$$

Now let

$$g(E',\varkappa) = f(E',E'-\varkappa)$$
$$= f(E+\varkappa,E) \quad .$$

Expanding $g(E',\varkappa)$ in a Taylor series about $E' = E$ while holding $\varkappa$ constant gives

$$g(E',\varkappa) = g(E,\varkappa) + \varkappa \left\{\frac{\partial}{\partial E'} [g(E',\varkappa)]\right\}_{E'=E} \quad .$$

Then

$$g(E',\varkappa) = g(E,\varkappa) + \varkappa \frac{\partial}{\partial E} [g(E,\varkappa)] \quad ,$$

so that

$$f(E',E'-\varkappa) = f(E,E-\varkappa) + \varkappa \frac{\partial}{\partial E} [f(E,E-\varkappa)] \quad ,$$

or

$$f(E+\varkappa,E) = f(E,E-\varkappa) + \varkappa \frac{\partial}{\partial E} [f(E,E-\varkappa)] \quad . \tag{39}$$

Substituting Eq. (39) into Eq. (38), and noting that $\varkappa$ and $\hat{\varkappa}$ are variables of integration so that the distinction between them may be dropped,

$$T = n \int_0^{I'} d\varkappa \, \varkappa \frac{\partial}{\partial E} [f(E,E-\varkappa)] \quad .$$

Now set $E' = E - \varkappa$, and

$$T = n \int_0^{I'} d\varkappa \, \varkappa \frac{\partial}{\partial E} \left[\frac{d\sigma(E,E')}{dE'} \phi(\vec{R},E,\vec{\Omega})\right] \quad . \tag{40}$$

Defining the stopping power S(E) as

$$S(E) = n \int_{o}^{I'} d\varkappa \, \varkappa \, \frac{d\sigma(E,E')}{dE'} \quad , \tag{41}$$

or

$$S(E) = n \int_{E-I}^{E} dE' \, (E-E') \, \frac{d\sigma(E,E')}{dE'} \quad . \tag{42}$$

Then substitute Eq. (41) into Eq. (40), to find

$$T = \frac{\partial}{\partial E} [S(E) \, \phi(\vec{R},E,\vec{\Omega})] \quad . \tag{43}$$

Equation (42) defines the relationship between the stopping power and the differential cross section for low-energy transfer collisions. As initially defined in Eq. (35), T represents two terms in Eq. (34). T as defined by Eq. (43) is now substituted back into Eq. (34) to give

$$\begin{aligned} \vec{\Omega}.\nabla\phi(\vec{R},E,\vec{\Omega}) = P(\vec{R},E,\vec{\Omega}) &+ n \int_{E}^{E_o} dE' \int d\Omega' \, \frac{d^2\sigma^*_{e\to e}(E',E,\vec{\Omega}'\cdot\vec{\Omega})}{dEd\Omega} \, \phi(\vec{R},E',\vec{\Omega}') \\ &- n \, \sigma^*_{e\to e}(E) \, \phi(\vec{R},E,\vec{\Omega}) \\ &+ n \int_{E+I'}^{E_o} dE' \int d\Omega' \, \frac{d^2\sigma_{inel}(E',E,\vec{\Omega}'\cdot\vec{\Omega})}{dEd\Omega} \, \phi(\vec{R},E',\vec{\Omega}') \\ &- n \, \sigma_1^T(E) \, \phi(\vec{R},E,\vec{\Omega}) + \frac{\partial}{\partial E} [S(E) \, \phi(\vec{R},E,\vec{\Omega})] \quad . \end{aligned} \tag{44}$$

The low-energy transfer collisions represented by $\frac{\partial}{\partial E} [S(E) \, \phi(\vec{R},E,\vec{\Omega})]$ in Eq. (44) now do not produce knock-on electrons but only reduce the energy of the incident electron.

Equation (44) is given in Section III as Eq. (16), with S(E) defined as in Eq. (42), and is the form of the transport equation solved by AWCS (ANISN with continuous slowing down used to treat low-energy transfer collisions).

APPENDIX B

HIGH-FREQUENCY END-POINT CORRECTION FOR THE DIFFERENTIAL BREMSSTRAHLUNG CROSS SECTION

The bremsstrahlung cross section of McCormick, Keiffer, and Parzen,[37] which is differential in angle and energy, was given as Eq. (30) in Section IV. When Eq. (30) is integrated over angle, the result may be expressed as "Eq. (3BN)" in Koch and Motz:[16]

$$d\sigma_k = \frac{Z^2 r_o^2}{137}\frac{dk}{k}\frac{p}{p_o}\left\{\frac{4}{3} - 2E_oE\left(\frac{p^2+p_o^2}{p^2\,p_o^2}\right) + \frac{\varepsilon_o E}{p_o^3} + \frac{\varepsilon E_o}{p^3} - \frac{\varepsilon\,\varepsilon_o}{p_o p}\right.$$

$$+ L\left[\frac{8E_oE}{3p_op} + \frac{k^2(E_o^2E^2+p_o^2p^2)}{p_o^3p^3} + \frac{k}{2p_op}\left(\left(\frac{E_oE+p_o^2}{p_o^3}\right)\varepsilon_o\right.\right. \tag{45}$$

$$\left.\left.\left. - \left(\frac{E_oE+p^2}{p^3}\right)\varepsilon + \frac{2kE_oE}{p^2p_o^2}\right)\right]\right\},$$

where

$$L = 2\ln\left[\frac{E_oE + p_op-1}{k}\right],$$

$$\varepsilon_o = \ln\left(\frac{E_o+p_o}{E_o-p_o}\right),$$

$$\varepsilon = \ln\left(\frac{E+p}{E-p}\right),$$

E_o, E = the initial and final total energy of the electron in a collision, in mc^2 units,

p_o, p = the initial and final momentum of the electron in a collision, in mc units,

k = the energy of the emitted photon in mc^2 units.

The bremsstrahlung cross section should have a finite value at the high-frequency limit, but Eq. (45) gives a value which approaches 0 as $p \to 0$. Fano's cross-section formula for the high-frequency limit is given by Koch and Motz [in Eq. (II-9)] as:

$$d\sigma_k = 4\pi \frac{Z^3 r_o^2}{137^2} \frac{dk}{k} \frac{E_o \beta_o}{(E_o-1)^2} \left\{ \frac{4}{3} + \frac{E_o(E_o-2)}{(E_o+1)} \left[1 - \frac{1}{2\beta_o E_o^2} \ln \frac{1+\beta_o}{1-\beta_o} \right] \right\}, \qquad (46)$$

where

β_o, β = the ratio of the initial and final electron velocity to the velocity of light.

A high-frequency limit correction factor F is sought, therefore, so that $d\sigma_k$ [Eq. (45)] $\times$ F = $d\sigma_k$ [Eq. (46)] when $p=0$. The form of the factor was chosen to be $F = \frac{X}{1-\exp(-X)}$, so that the correction would also apply near the limit, as $p \to 0$. Then

$$F = \frac{X}{1-\exp(-X)}, \qquad p \neq 0 ;$$

$$F = X, \qquad p = 0 .$$

Therefore, Eq. (45) must be evaluated as $p \to 0$ so the result set equal to Eq. (46) in order to find X. First multiply Eq. (45) by the factor X in the form $X = X'E/p$, and take the limit as $p \to 0$, to get

$$d\sigma_k = \frac{2Z^2 r_o^2}{137} \frac{dk}{k} \frac{X'}{p_o} \left[\frac{3E_o^4+E_o^3-E_o^2+7E_o+6}{3(E_o+1)(E_{o-1})E_o} \right] . \tag{47}$$

Then substitute the identities $2\beta_o \simeq \ln\left(\frac{1+\beta_o}{1-\beta_o}\right)$ and $p_o = \beta_o E_o$ into Eq. (46) to give

$$d\sigma_k = \frac{4\pi Z^3 r_o^2}{137^2} \frac{dk}{k} \left\{ \left(\frac{p_o}{(E_o-1)^2} \right) \left[\frac{4}{3} + \frac{(E_o-1)(E_o-2)}{E_o} \right] \right\} . \tag{48}$$

Now set Eq. (47) equal to Eq. (48) and solve for X', noting that $p_o^2+1 = E_o^2$, so that

$$X' = \frac{2\pi Z}{137} ,$$

and

$$X = \frac{2\pi ZE}{137p} ,$$

as given in Eq. (30), Section IV. This factor was derived to assure the correct value as $p \to 0$ after integration over angle, but it does not assure the correct limit at a specific angle.

ACKNOWLEDGMENTS

The authors are indebted to Dr. Y. Shima, whose present address is the Soreq Nuclear Research Center, Yavne, Israel, for aiding in programming the cross sections, to Dr. J. R. Knight and Mr. L. R. Williams for supplying the photon cross sections, and to Dr. F. S. Alsmiller for reviewing the manuscript.

REFERENCES

1. Proceedings of the Symposium on the Protection Against Radiation Hazards in Space, Gatlinburg, Tennessee, November 5-7, 1962, TID-7652, Office of Technical Services, Department of Commerce, Washington (1962). See, for example, J. A. Van Allen, "Brief Note on the Radiation Belts of the Earth," p. 1, Book 1, and S. L. Russak, "Radiation Dosages from Electrons and Bremsstrahlung in the Van Allen Belt," p. 760, Book 2.

2. Second Symposium on Protection Against Radiations in Space, Gatlinburg, Tennessee, October 12-14, 1964, National Aeronautics and Space Administration report NASA SP-71 (1965). See, for example, M. J. Berger and S. M. Seltzer, "Results of Some Recent Transport Calculations for Electrons and Bremsstrahlung," p. 437, and G. D. Magnuson and A. W. McReynolds, "Space Electron Radiation Shielding - Bremsstrahlung and Electron Transmission "p. 455.

3. M. J. Berger and S. M. Seltzer, "ETRAN Monte Carlo Code System for Electron and Photon Transport Through Extended Media," National Bureau of Standards Reports NBS-9836 (1968) and NBS-9837 (1968).

4. R. D. Birkhoff, p. 53 in Handbuch der Physik, Ed. by S. Flugge, Vol. 34. Berlin: Springer-Verlag (1968).

5. C. D. Zerby and F. S. Keller, Nucl. Sci. Eng. 27, 190 (1967).

6. H. A. Bethe, Phys. Rev. 89, 1256 (1953).

7. G. Moliere, Z. Naturforsch. 3a, 78 (1948).

8. S. A. Goudsmit and J. L. Saunderson, Phys. Rev. 57, 24, and Phys. Rev. 58, 36 (1940).

9. F. Rohrlich and B. C. Carlson, Phys. Rev. 93, 38 (1954).

10. E. J. Williams, Proc. Roy. Soc. (London) 125, 420 (1929).

11. L. Landau, J. Exp. Phys. (USSR), 8, 201 (1944).

12. L. V. Spencer and U. Fano, Phys. Rev. 93, 1172 (1954).

13. O. Blunck and S. Leisengang, Z. Physik 128, 500 (1950).

14. M. J. Berger and S. M. Seltzer, "Studies in Penetration of Charged Particles in Matter," National Research Council Report 39, Publication 1133, 187 (1964).

15. P. V. Vavilov, Zh. Eksp. Teor. Fiz. 32, 320 (1957), Transl., JETP 5, 749 (1957).

16. H. W. Koch and J. W. Motz, Rev. Mod. Phys. 31, 920 (1959).

17. C. Møller, Ann. Physik 14, 531 (1932).

18. M. J. Berger, "Monte Carlo Calculation of the Penetration and Diffusion of Fast Charged Particles," p. 135 in Methods in Computational Physics, Ed. by B. Adler, S. Fernbach, and M. Rotenburg, Vol. I. New York: Academic Press (1963).

19. M. Clark and K. F. Hansen, Numerical Methods of Reactor Analysis. New York: Academic Press (1964).

20. G. C. Wick, Z. Physik 121, 702 (1943).

21. B. C. Carlson, "Solution of the Transport Equation by S_n Approximation," Los Alamos Scientific Laboratory Report LA-1891 (1955).

22. B. C. Carlson, "Numerical Solution of Neutron Transport Problems," p. 219 in Proc. Eleventh Symposium in Applied Mathematics, American Mathematical Society, Providence, R. I. (1961).

23. W. W. Engle, Jr., "A Users Manual for ANISN, a One-Dimensional Discrete Ordinates Transport Code with Anisotropic Scattering," Computing Technology Center, Union Carbide Corporation, Report K-1693 (1967).

24. F. R. Mynatt, F. J. Muckenthaler, and P. N. Stevens, "Development of Two-Dimensional Discrete Ordinates Transport Theory for Radiation Shielding," Computing Technology Center, Union Carbide Corporation, Report CTC-INF-952 (1969).

25. D. H. Rester and W. J. Rainwater, "Investigations of Electron Interactions with Matter," National Aeronautics and Space Administration Report CR-334 (1965).

26. D. H. Rester and W. E. Dance, "Investigations of Electron Interactions with Matter," Ling-Temco-Vought, Inc. Report No. 0-71000/6R-18 (1966).

27. J. A. Lonergan, C. P. Jupiter, and G. Merkel, J. Appl. Phys. 41, 678 (1970).

28. K. D. Lathrop, "DTF-IV, a FORTRAN-IV Program for Solving the Multigroup Transport Equation with Anisotropic Scattering," Los Alamos Scientific Laboratory Report LA-3373 (1965).

29. S. A. Dupree, H. A. Sandmeier, G. E. Hansen, W. W. Engle, and F. R. Mynatt, "Time-Dependent Neutron and Photon Transport Calculations Using the Method of Discrete Ordinates," Los Alamos Scientific Laboratory Report LA-4557, (ORNL-4662), (SAI-70-125), (1971).

30. M. J. Berger and S. M. Seltzer, "Tables of Energy Losses and Ranges of Electrons and Positrons," National Aeronautics and Space Administration Report N65-12506 (1964).

31. B. Rossi, High Energy Particles. Englewood Cliffs: Prentice-Hall (1952).

32. H. A. Bethe, p. 273 in Handbuch der Physik, Vol. 24, 2d ed. Berlin: Springer-Verlag (1933).

33. R. M. Sternheimer, Phys. Rev. 103, 511 (1956).

34. N. F. Mott, Proc. Roy. Soc. (London) A135, 429 (1932).

35. J. A. Doggett and L. V. Spencer, Phys. Rev. 103, 1597 (1956).

36. L. V. Spencer, Phys. Rev. 98, 1507 (1955).

37. P. T. McCormick, D. G. Keiffer, and G. Parzen, Phys. Rev. 103, 29 (1956).

38. G. Racah, Nuovo Cimento 11, 476 (1934).

39. J. R. Knight and F. R. Mynatt, "MUG, a Program for Generating Multigroup Photon Cross Sections," Oak Ridge National Laboratory Report CTC-17 (1970).

40. R. D. Evans, The Atomic Nucleus. New York: McGraw-Hill (1955).

41. W. H. McMaster, N. Kerr Del Grande, J. H. Mallett, and J. H. Hubbell "Compilation of X-Ray Cross Sections," Lawrence Radiation Laboratory Report UCRL-50174, Sec. II, Rev. 1 (1969).

42. E. F. Plechaty and J. R. Terrall, "Photon Cross Sections 1 keV to 100 MeV," Lawrence Radiation Laboratory Report UCEL-50400, Vol. VI (1968).

43. C. Passow, Deutches Elektronen-Synchrotron, Hamburg, Germany, "Phanomenologishe Theory Zur Berechnung einer Kasdade aus Schweren Teilchen (Nukleonkascade) in der Materie," DESY-Notiz A2.85 (1962)

44. F. S. Alsmiller, "A General Category of Soluble Nucleon-Meson Cascade Equations," Oak Ridge National Laboratory Report ORNL-3746 (1965).

45. F. B. Hildebrand, Advanced Calculus for Applications. Englewood Cliffs: Prentice-Hall (1965), p. 150.

46. D. H. Rester, "Comparisons of Experimental and Calculated Electron Transmission and Bremsstrahlung Spectra for Electron Energies Below 3.0 MeV," Ling-Temco-Vought, Inc. Report No. 0-71100/OR-6 (1970).

47. D. H. Rester and J. H. Derrickson, J. Appl. Phys. 42, 714 (1971)

48. W. W. Scott, "Comparisons of the Results Obtained with Several Electron-Penetration Codes," Oak Ridge National Laboratory Report ORNL RSIC-28 (1970).

49. R. E. Carter, F. Reines, J. J. Wagner, and M. E. Wyman, Phys. Rev. 113, 280 (1959).

50. F. R. Mynatt, Trans. Am. Nucl. Soc. 12, 260 (1970).

Internal Distribution

1-3. L. S. Abbott
4. F. S. Alsmiller
5-24. R. G. Alsmiller, Jr.
25. T. W. Armstrong
26. J. Barish
27-36. D. E. Bartine
37. H. W. Bertini
38. C. E. Clifford
39. W. W. Engle, Jr.
40. T. A. Gabriel
41. M. P. Guthrie
42. W. E. Kinney
43. T. A. Love
44. F. C. Maienschein
45. F. R. Mynatt
46. R. W. Peelle
47. R. W. Roussin
48. R. T. Santoro
49. D. Sundberg
50. J. A. Turner
51. J. W. Wachter
52. H. A. Wright
53. W. Zobel
54. E. R. Cohen (consultant)
55. H. Feshbach (consultant)
56. H. Goldstein (consultant)
57. C. R. Mehl (consultant)
58. H. T. Motz (consultant)
59-60. Central Research Library
61. ORNL Y-12 Technical Library, Document Reference Section
62-63. Laboratory Records Department
64. Laboratory Records ORNL RC
65. ORNL Patent Office

External Distribution

66. Major R. W. Enz, Air Force Weapons Laboratory, Kirtland Air Force Base, New Mexico, 87117.
67. P. B. Hemmig, Division of Reactor Development & Technology, U. S. Atomic Energy Commission, Washington, D. C.
68. W. H. Hannum, Division of Reactor Development & Technology, U. S. Atomic Energy Commission, Washington, D. C.
69. Kermit Laughon, AEC Site Representative.
70. Y. Shima, Soreq Nuclear Research Center, Yavne, Israel.
71-160. Given NASA Space Shielding Distribution.*
161-162. Division of Technical Information (DTIE).
163. Laboratory and University Division (ORO).

*This distribution list is available upon request.